Supporting Information

Scalable Mechanochemical Synthesis of High-quality Prussian Blue Analogues for High-Energy and Durable Potassium-Ion Batteries

Xunan Wang[a], Chongwei Gao[a], Shuhua Zhang[a], Jiantao Li[b], Jiali Wang[a], Shengdong Lin[a], Sungsik Lee[c], Feiyu Kang[a] and Dengyun Zhai[a]**

[a] Institute of Materials Research, Tsinghua Shenzhen International Graduate School, Tsinghua University, Shenzhen 518055, China.

E-mail: fykang@mail.tsinghua.edu.cn, zhaidy0404@sz.tsinghua.edu.cn

[b] Chemical Sciences and Engineering Division, Argonne National Laboratory, Lemont, Illinois 60439, USA.

[c] X-ray Science Division, Advanced Photon Source, Argonne National Laboratory, Lemont, Illinois 60439, USA.

KEYWORDS: Mechanochemical method, Prussian blue analogues, $[Fe(CN)_6]^{4-}$ vacancy, Potassium-ion batteries, High-energy and durable

Experimental Section

Materials Synthesis: For KMnF-MC, $MnCl_2$ and $K_4[Fe(CN)_6]$ were used to synthesize the target product $K_2Mn[Fe(CN)_6]$ (KMnF-MC). Then, stoichiometric amounts of $MnCl_2$ and $K_4[Fe(CN)_6]$ (mole ratio = 1/1) and a certain amount of 5 mm zirconia balls (weight ratio about 1:10) were put into the bowl of planetary ball mill (Pulverisette 7; Fritsch) and were ball-milled at 500 r.p.m. for 10 minutes. After the reaction was completed, the product was collected by centrifuge and washed once with deionized water, and then dried by a vacuum dryer. There was no pretreatment before the use of synthetic raw materials, and all operation was carried out at room temperature and atmospheric atmosphere. For the $K_2Mg[Fe(CN)_6]$ and $K_2Ca[Fe(CN)_6]$, Mn in the raw material is replaced with Mg or Ca.

The KMnF-CP was obtained by co-precipitation method according previous reports. Typically, 4 mmol $MnCl_2$ (with 4 mmol potassium citrate) and 4 mmol $K_4[Fe(CN)_6]$ were dissolved in 100 mL deionized water to obtain solution A and solution B, respectively. Slowly dropped solution A into solution B and stir magnetically for 24 h to achieve full nucleation and growth. After the end of the reaction, the suspension was left to stand for 12 hours to better collect the precipitated products. The precipitate was collected by centrifuging and washed with deionized water for three times, followed by final drying at 100 °C overnight in vacuum. For the $K_2Mg[Fe(CN)_6]$ and $K_2Ca[Fe(CN)_6]$, Mn in the raw material is replaced with Mg or Ca.

Materials Characterizations: The XRD (Rigaku D/max 2500/PC, Cu-Ka, $\lambda = 0.154$ nm) patterns were tested to characterize the crystal structure of PBAs. The HRTEM images and EDS elemental mappings were recorded using High-resolution Transmission Electron Microscopy (HRTEM, FEI Tecnai G2 F30). Scanning electron microscope (SEM) was performed using a HITACHI SU8010.EPR spectra were recorded from Bruker EMXplus-6/1 EPR spectrometer (9065.8 MHz, X band, 300 K). XAS measurements were collected at 12-BM-B at the Advanced Photon Source (APS) in Argonne National Laboratory. The radiation was monochromatized by a Si (111) double-crystal monochromator. The chemical composition of samples was tested by

Thermogravimetric analysis (TGA) and Inductive Coupled Plasma Emission Spectroscopy (ICP-OES). The TGA-MS results were tested at a heating rate of 10 °C min^{-1} under N_2 gas flow from 25-650 °C. Fourier transform infrared spectroscopy (FTIR) was performed using a Nicolet iS50. Raman spectra were collected by a Raman spectrometer (Horiba LabRAM HR800). The X-ray Photoelectron Spectroscopy (XPS) analysis was conducted on a PHI 5000 VersaProbe II using a monochromatic Al Kα radiation. In-suit variable temperature XRD measurement was performed from 100 °C to 450 °C under N_2 gas flow at 25 °C intervals. The in-situ electrochemical XRD was measured in a custom-made module cell within the 2θ angle range of 15–38° upon charging-discharging the KMnF//K cell at 0.2 C.

Electrochemical Measurements: The KMnF and PTCDI slurry were obtained by stirring the active materials, conductive carbon, polyvinylidene fluoride (PVDF) in a weight ratio of (7:2:1). The loading mass of cathode was ≈ 1 mg cm^{-2}. The graphite anode was fabricated by spreading the slurry of active materials, conductive carbon, and carboxymethyl cellulose sodium (weight ratio of 8:1:1).

Typical 3 M KFSI in DME was used as electrolytes for K^+ storage. All the CR2032-type coin cells were assembled in a Braun glove box under an Ar atmosphere with contents of oxygen and moisture below 0.1 ppm. In order to avoid FSI^- anion corrosion of traditional stainless steel, we used aluminum-clad coin cells (Guangdong Canrd New Energy Technology Co. Ltd) for the tests. For the K metal cell tests, using K metal as the counter electrode, one piece of Celgard 2320 plus one piece of glass microfiber filter (GF/D) as separator, with an electrolyte dosage of 30 μL. To eliminate the initial irreversible capacity of the anode, the graphite//K half cell was discharged-charged for 5 cycles at 0.1 C between 0.01-2.0 V (vs. K^+/K) before assembling the full cell. To construct the full cell, the capacity ratio of KMnF-MC: Gr is set to be ≈ 1:1.2 (≈1:0.65 of mass ratio). For KMnF-MC//PTCDI full cells (N/P is set to 1.1), fresh positive and negative direct assembly does not require pre-cycling.

For the pouch cell, the preparation of positive electrode (KMnF-MC) and negative electrode (PTCDI) with high mass loading was carried out by dry electrode preparation process, and the weight ratio of active material to carbon black and polytetrafluoroethylene was set to 8:1:1. The positive electrode was cut into a size of about 3 × 4 cm^2 with 16.5 mg cm^{-2}, while the negative electrode was fabricated with slightly larger dimensions of 3.2 × 4.2 cm^2 and a high loading of 20.6 mg cm^{-2} (N/P ratio ≈1.1). The thickness and surface morphology of both positive and negative electrodes were systematically characterized, as illustrated in Figures S43 and 44. The pouch cell was designed in a single-layer configuration, employing a glass microfiber filter (GF/A, 3.5 × 4.5 cm^2) as the separator, with an electrolyte dosage of 300 µL. The detailed assembly description of the pouch cell is schematically presented in Figure S45.

The Cyclic Voltammetry (CV) tests and Electrochemical impedance spectroscopy (EIS; with frequency from 100 kHz to 10 mHz at an amplitude of 10 mV) were obtained with VMP-3 multichannel workstation. The in-situ EIS was tested using homemade three-electrode coin cells (KMnF//K_{CE}//K_{RE}, Figure S28) with equal proportional capacity intervals. The distribution of relaxation times (DRT) was calculated from the EIS data using MATLAB script-based software. The galvanostatic intermittent titration technique (GITT) was used to determine the diffusion coefficients of K^+ in different materials. Before GITT measurements, cells were initially activated for 3 cycles at 0.5 C, and subsequently charged or discharged for 10 min at a pulse current of 20 mA g^{-1}, followed by a duration of 20 min relaxation to achieve K^+ equilibrium potential.

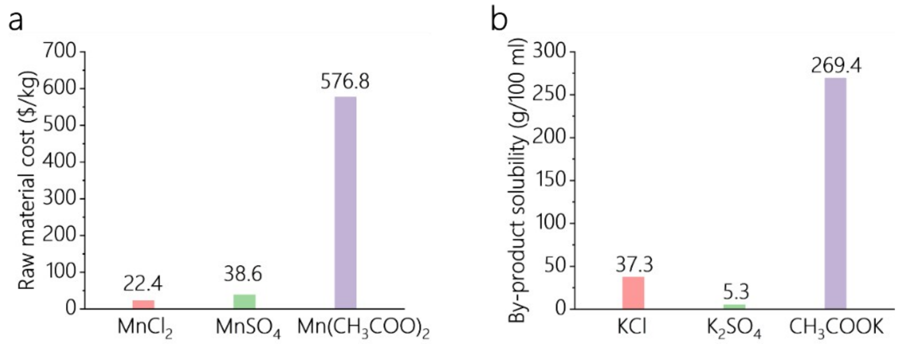

Figure S1. (a) Typical manganese salt prices and (b) corresponding by-product solubility.

The corresponding reaction equation can be defined as Equation S1 below:

$$K_4[Fe(CN)_6] + MnCl_2 \rightarrow K_2Mn[Fe(CN)_6] + 2KCl, \quad \text{Equation S1}$$

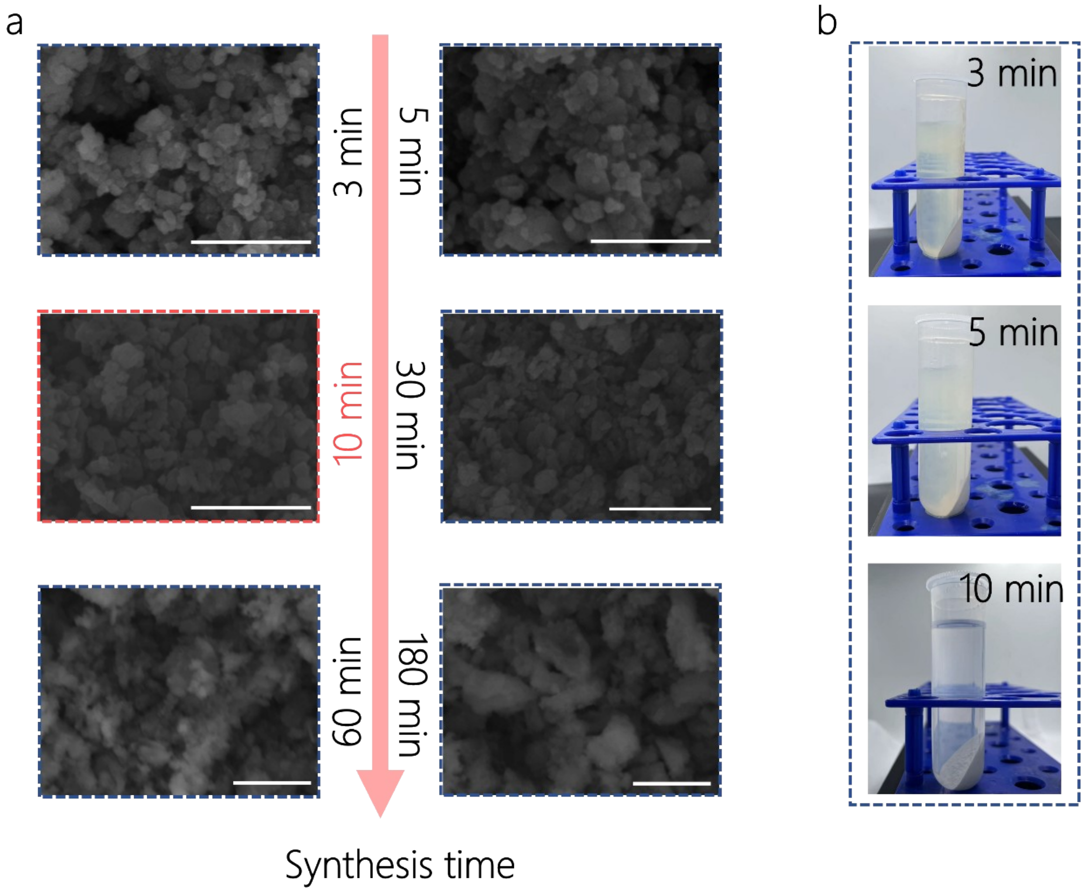

Figure S2. (a) The scanning electron microscopy (SEM) images of KMnF-MC synthesized at different times. (b) Centrifugation to collect photographs of the resulting product and supernatant. Scale bars in panels a are 500 nm.

The KMnF-MC product was collected in 3 minutes of the HEBM reaction, but the supernatant was yellowish and correspondingly $K_4[Fe(CN)_6]$ remaining, indicating that the reaction was not complete. The reaction was carried out to 10 minutes, and the supernatant overnight after centrifugation became colorless, and the particle morphology was uniform. The reaction time was extended to 30 minutes, and the obtained product is similar to sample prepared in 10 minutes. As the reaction time is extended to 1 hour, the KMnF particles begin to agglomerate.

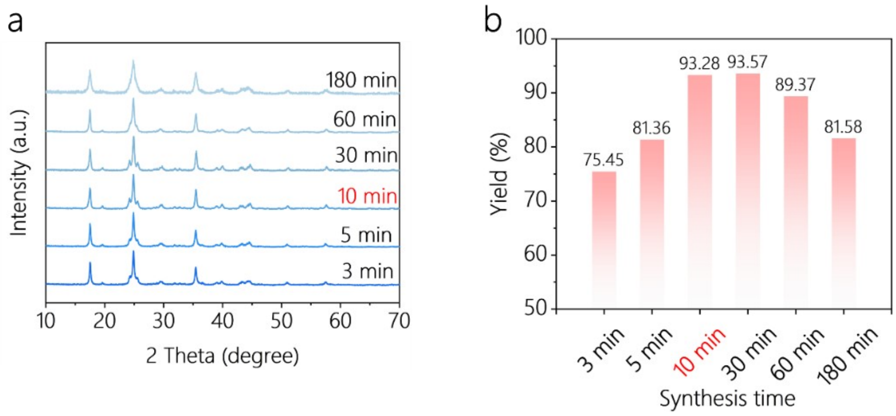

Figure S3. (a) The XRD patterns of KMnF-MC synthesized at different times. (b) The yields of KMnF samples obtained from different reaction time.

The crystallinity of the synthesized samples material first increases and then decreases with the extension of the reaction time. And the excessive reaction time using HEBM may cause local overheating and stress [1, 2]. When the reaction time is between 10 and 30 minutes, the crystallinity and the yield of KMnF-MC is optimal. Combined with the concern on energy consumption, the reaction time of 10 minutes was selected.

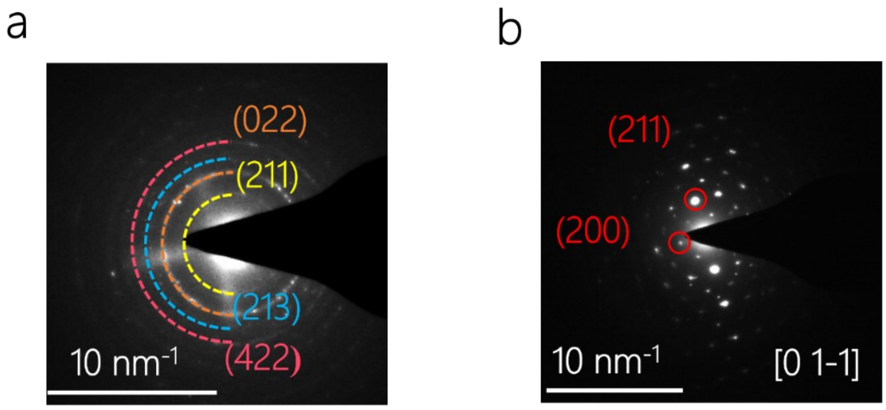

Figure S4. Selective area electron diffraction (SAED) patterns for (a) Polycrystalline and (b) single-crystal areas of the KMnF-MC.

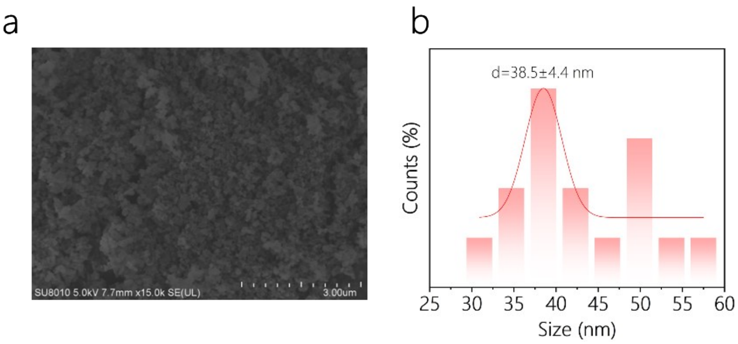

Figure S5. (a) The SEM images at different magnifications and (b) particle size distribution statistics of KMnF- MC.

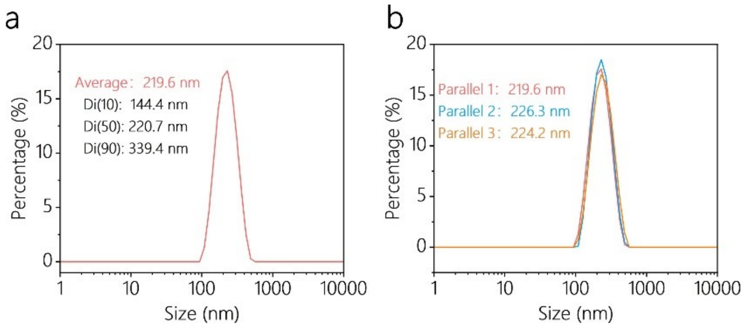

Figure S6. (a) Particle size distribution of KMnF-MC. (b) Corresponds to the results of three parallel tests.

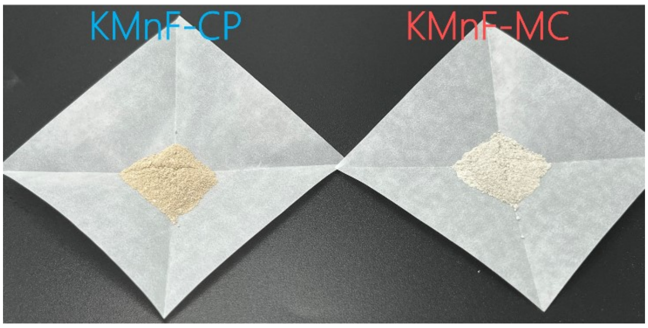

Figure S7. Digital photograph of the KMnF-CP and KMnF-MC power.

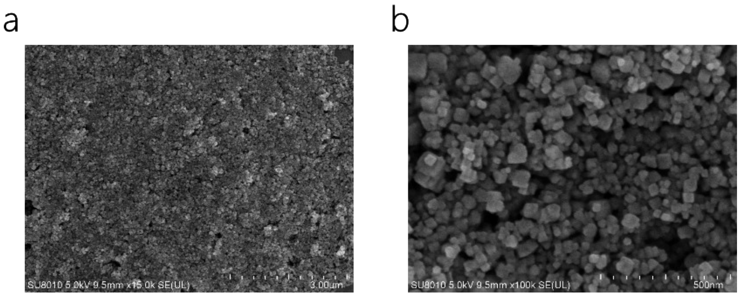

Figure S8. (a), (b) The SEM images at different magnifications of KMnF- CP.

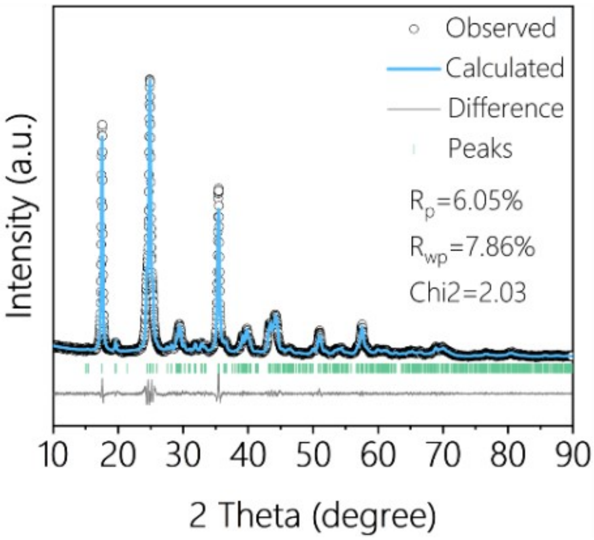

Figure S9. Rietveld-refined profiles of KMnF-CP.

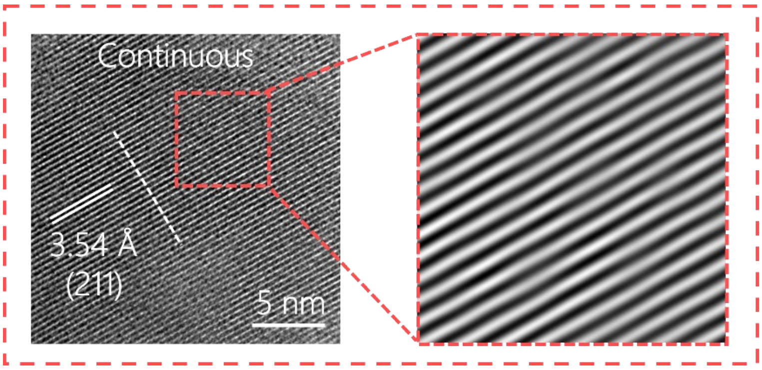

Figure S10. HRTEM image and the IFFT corresponding to the frame area of as-prepared KMnF-MC.

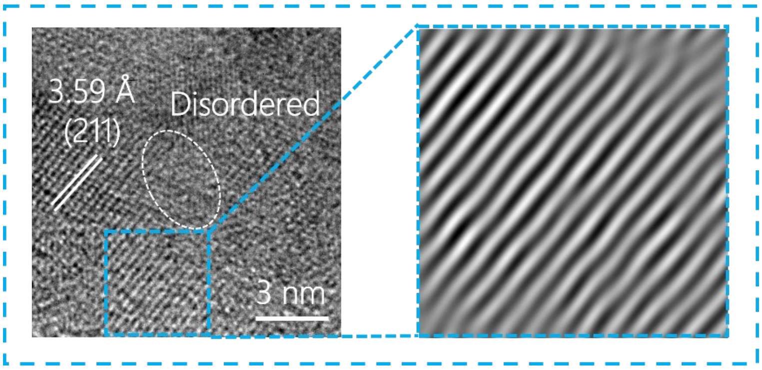

Figure S11. HRTEM image and the IFFT corresponding to the frame area of as-prepared KMnF-CP.

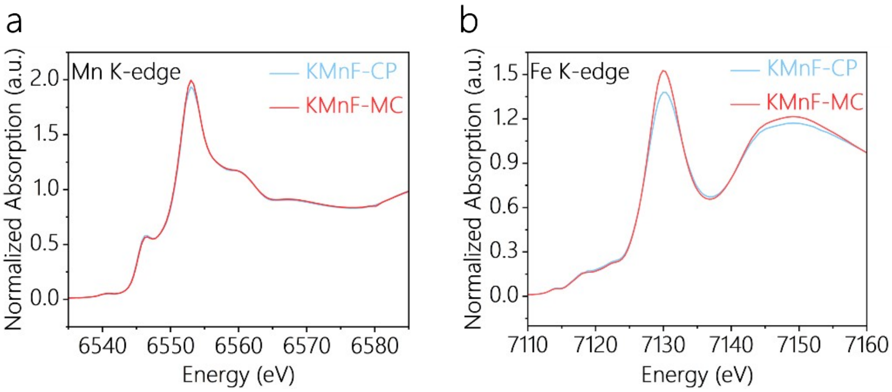

Figure S12. Normalized XANES spectra at the Mn K-edge (a) and Fe K-edge (b) of two samples.

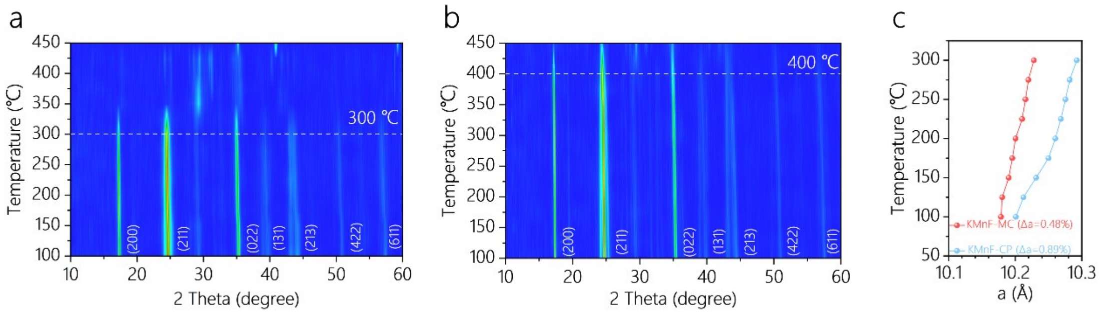

Figure S13. Operando phase transformation of the KMnF-CP (a) and KMnF-MC (b) samples during heating from 100 °C to 450 °C. (c) Comparison of the cell parameters changes of distorted framework of two samples during heating process.

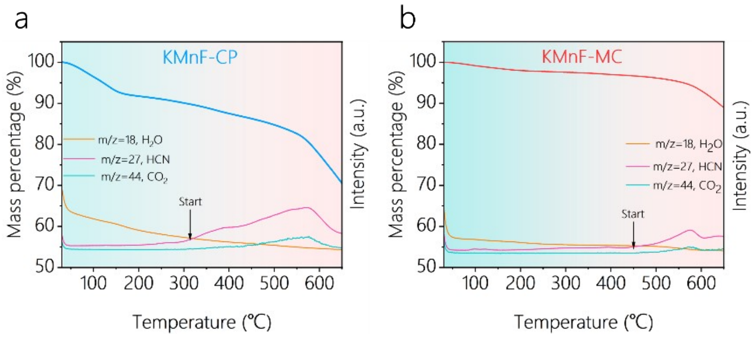

Figure S14. TGA-MS curves of the KMnF-CP (a) and KMnF-MC (b) samples tested in N_2.

The continuous weight loss and the change in the H_2O intensity signal between 25 and 260 °C can attributed to the removal of adsorbed water and lattice water[3]. It is worth noting that the temperature below 300 °C, no other gases are detected, indicating that the structure of two KMnF samples is maintained well and does not decompose. As the temperature continues to rise by more than 300 °C, HCN and CO_2 gas signals appear in KMnF-CP and impure phases are detected in XRD, indicating that the frame structure began to be destroyed[4, 5]. In contrast, KMnF-MC significantly delays the temperature at which gases and impurity are generated.

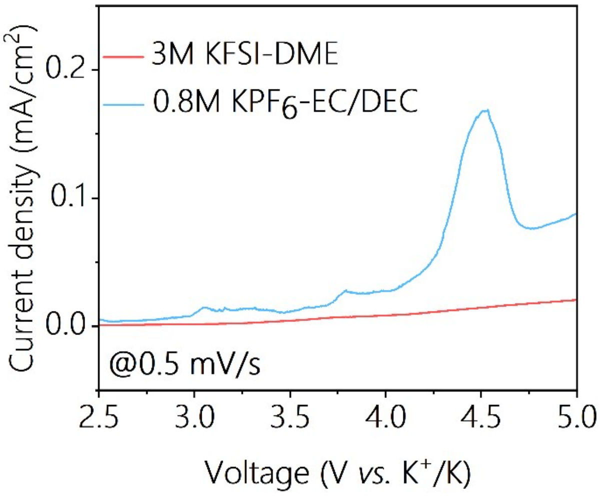

Figure S15. The linear sweep voltammetry (LSV) results of two electrolytes.

The linear sweep voltammetry (LSV) results (Figure S15) show an obvious current response at about 3.8 V of 0.8M KPF_6 EC/DEC, indicating that the electrolyte undergoes irreversible oxidative decomposition and cannot meet the charge/discharge of KMnF-MC at the 4.4 V high cut-off voltage.

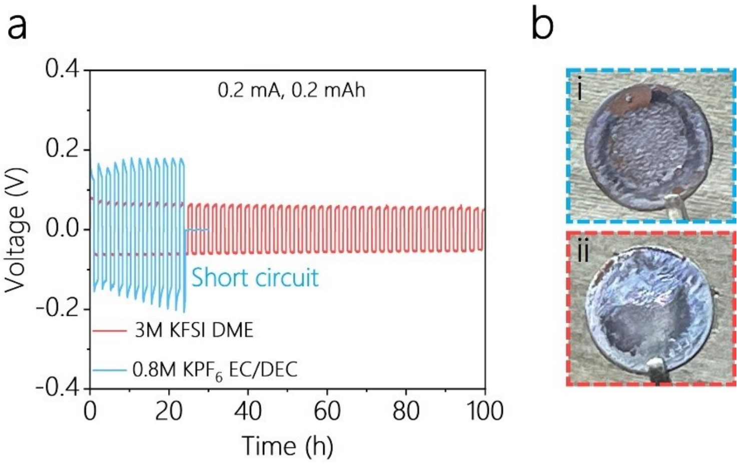

Figure S16. (a) The K//K symmetric cell testing. (b) The optical photographs of potassium metal deposition in (i) 0.8M KPF_6 EC/DEC and (ii) 3M KFSI DME.

As shown in Figure S16a, K//K symmetric cell employing the 0.8M KPF_6 EC/DEC electrolyte exhibits significantly larger voltage polarization and rapid short-circuiting behavior. Furthermore, electrochemical deposition of potassium metal on Cu foil in this electrolyte result in discontinuous and irregular metal morphology in Figure S16b (i). In contrast, the 3M KFSI in DME electrolyte overcomes these challenges. Therefore, the utilization of 3M KFSI DME electrolyte enables more reliable electrochemical evaluation of the intrinsic performance of cathode materials by minimizing interference from both potassium metal anode instability and electrolyte decomposition at high voltage.

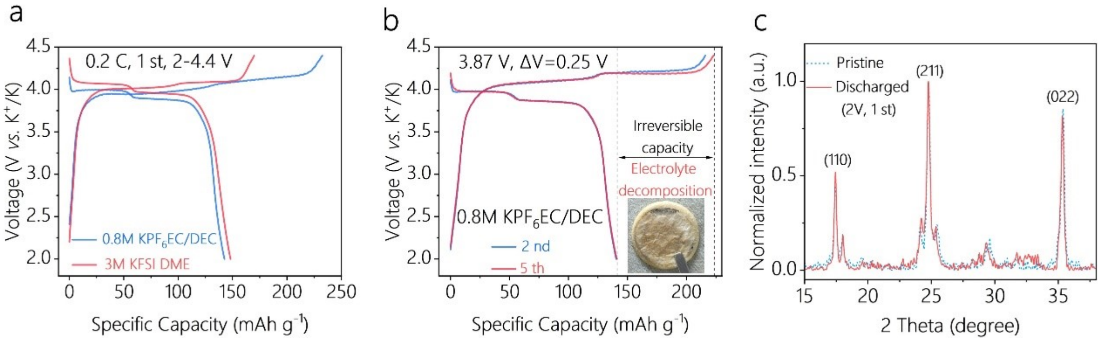

Figure S17. (a) The first galvanostatic charge–discharge voltage profiles of KMnF-MC at 30 mA g^{-1} (0.2 C, 1C=150 mA g^{-1}) with two electrolytes. (b) The 2nd-5th voltage profiles of KMnF-MC at 0.2 C tested with 0.8M KPF_6 EC/DEC electrolyte. Inset: optical photograph of the separator after 5 cycles. (c) XRD pattern of KMnF-MC before and after the initial cycle tested with 0.8M KPF_6 EC/DEC electrolyte.

As illustrated in Figure S17a, the KMnF-MC cathode demonstrates a notably low initial Coulombic efficiency of merely 61.3% in 0.8M KPF_6 EC/DEC electrolyte. Irreversible capacity (~35%) persists during substantial cycles (Figure S17b). In addition, the KMnF-MC cathode in 0.8M KPF_6 EC/DEC delivers both reduced capacity (141 vs. 149 mAh g^{-1}) and average voltage (3.87 vs. 3.96 V) than in 3M KFSI DME electrolytes (Figure S17b and Figure 3a), likely due to the higher polarization voltage associated with potassium metal deposition. The XRD was performed to examine the structural evolution of the cathode before and after the initial cycle (Figure R17c). The three strongest diffraction peaks fully return to initial state, confirming non-solvated K⁺ intercalation, as also observed in 3M KFSI DME electrolyte (see Figure 4a). These findings demonstrate that the K⁺ intercalation mechanism of KMnF cathode ("naked" K⁺) is independent of electrolyte choice, unlike graphite where electrolyte governs solvent co-intercalation. Furthermore, our manuscript has comprehensively demonstrated that the superior electrochemical performance of the KMnF-MC cathode originates from the high crystallinity, as evidenced by comparative analysis with KMnF-CP under identical electrolyte conditions (3M KFSI in DME).

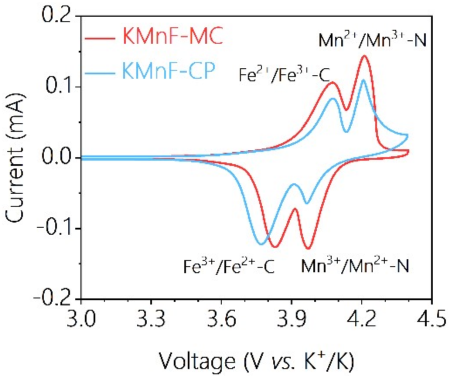

Figure S18. The cyclic voltammetry (CV) curves of the second cycle at 0.1 mV/s.

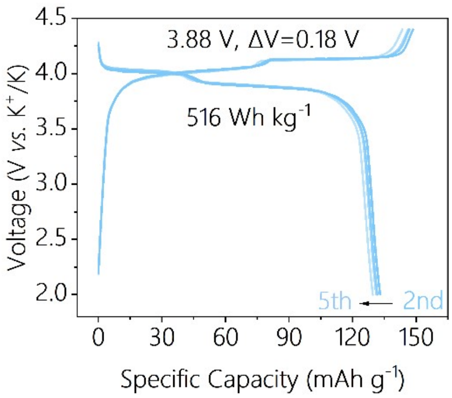

Figure S19. Galvanostatic charge/discharge voltage profiles of KMnF-CP at 30 mA g^{-1}.

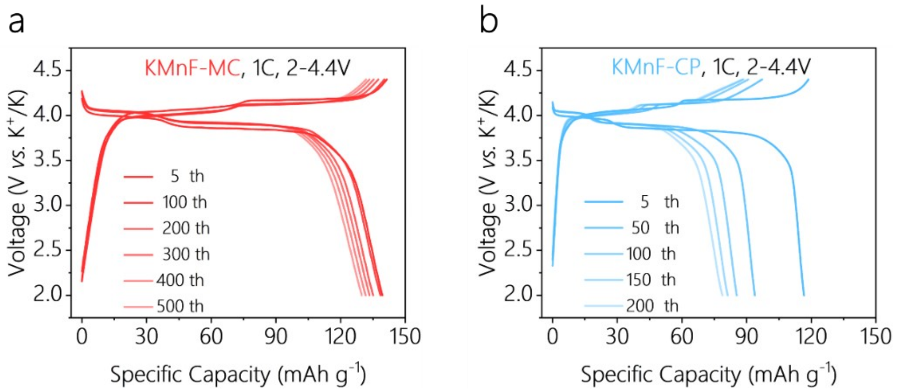

Figure S20. The voltage curves at 1 C (150 mA g^{-1}) of KMnF-MC for 500 cycles (a) and KMnF-CP for 200 cycles (b).

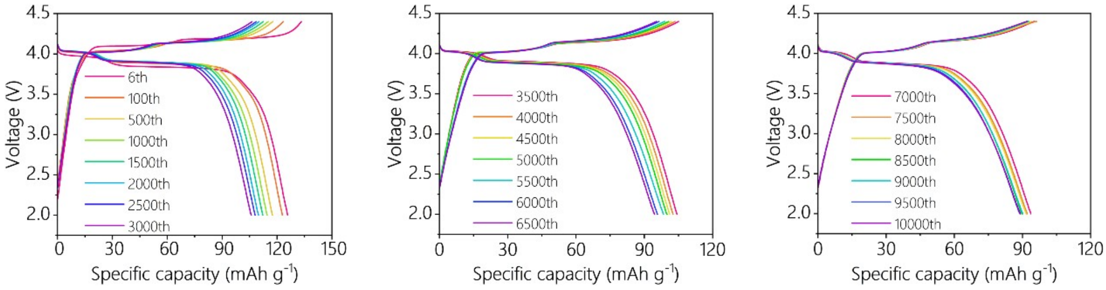

Figure S21. The voltage curves at 5 C (750 mA g^{-1}) of KMnF-MC for 10,000 cycles.

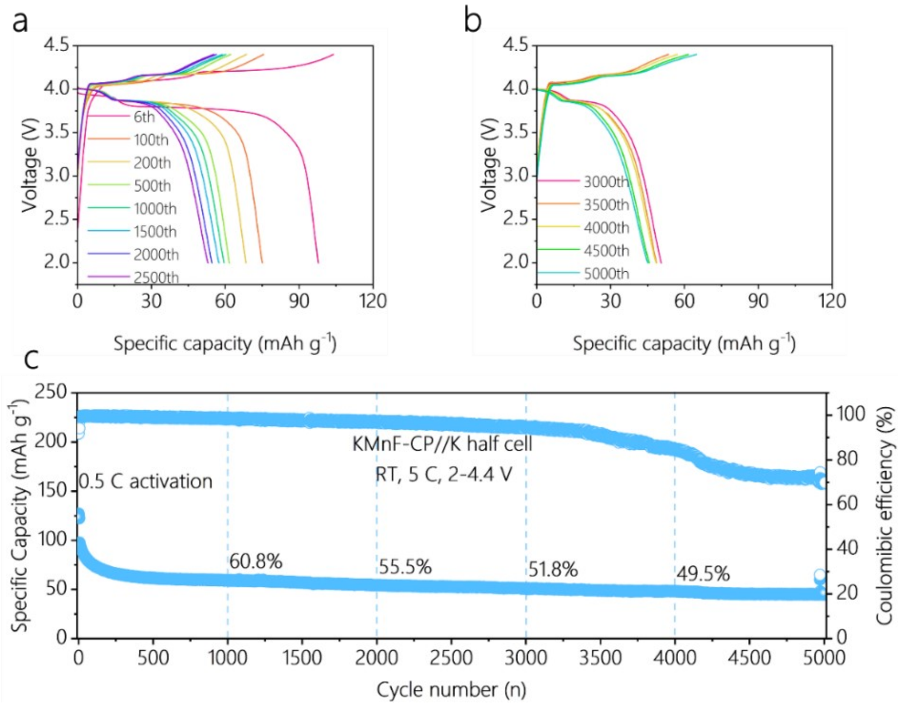

Figure S22. The voltage curves and cycle performance at 5 C (750 mA g^{-1}) of KMnF-CP for 5,000 cycles.

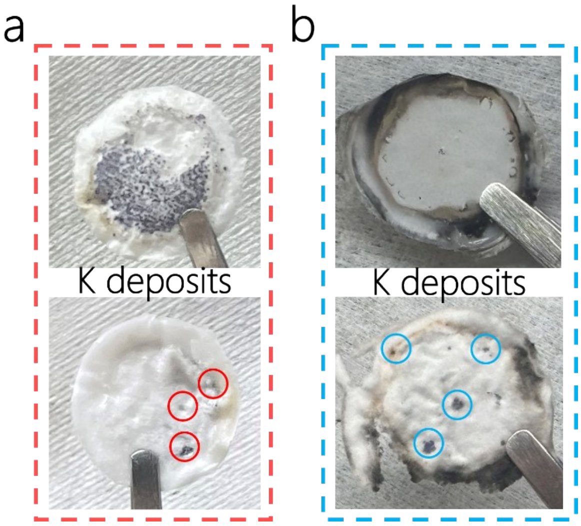

Figure S23. Digital photograph of the separator disassembled after 5,000 cycles of KMnF-MC (a) and KMnF-CP (b).

By comparing the separator after cycling, it can be conjectured that the fewer side reactions occurred in KMnF-MC//K cell, which is directly related to maintaining high capacity and coulombic efficiency. Notably, the apparent metal K deposits were detected in both cases. In order to avoid short-circuit failures caused by K deposition, the KMnF-MC//K cells were disassembled after 5,000 cycles and then reassembled.

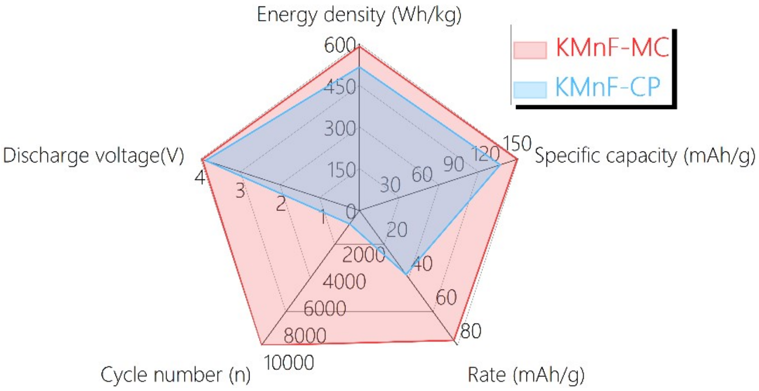

Figure S24. The specific capacity, discharge voltage, energy density, cycle numbers and rate performance of two samples are compared.

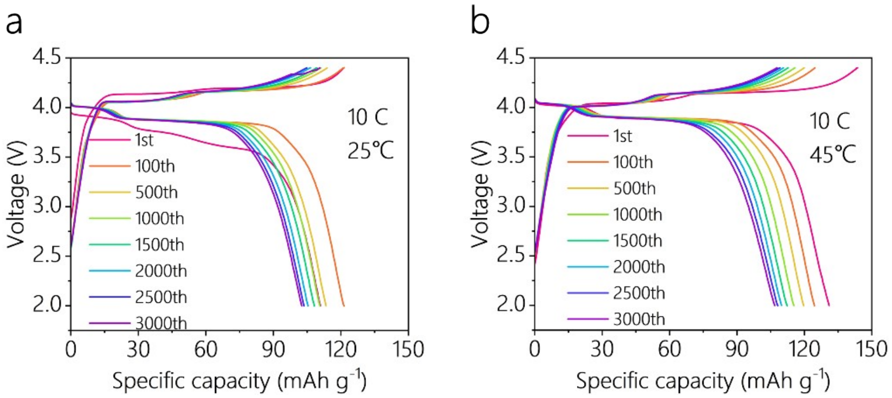

Figure S25. The voltage curves at 10 C (1,500 mA g^{-1}) of KMnF-MC for 3,000 cycles at 25 °C (a) and 45 °C (b).

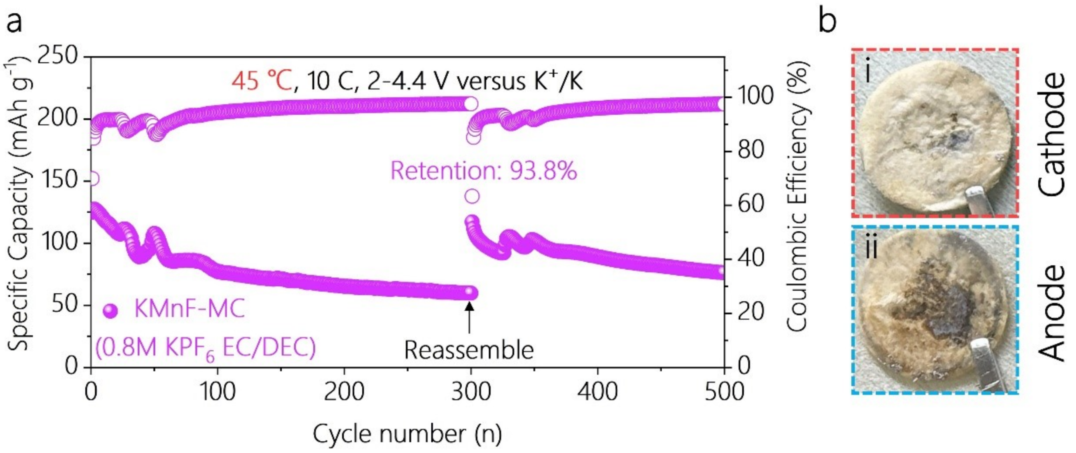

Figure S26. (a) The cycling performance of KMnF-MC under 45 °C tested with 0.8M KPF_6 EC/DEC electrolyte. (b) The optical photograph of the separator after 300 cycles.

The 0.8M KPF_6 EC/DEC electrolyte exhibits more severe decomposition at high voltages compared to 3M KFSI/DME (Figure S15), a phenomenon further exacerbated at elevated temperatures (45°C). As illustrated in Figure S26a, the KMnF-MC//0.8M KPF_6 EC/DEC//K cell shows rapid capacity decay and markedly lower Coulombic efficiency at 45°C than its counterpart using 3M KFSI/DME (Figure 3i). After 300 cycles, the separator showed near-total electrolyte depletion (Figure S26b), yet the reassembled cell recovered 93.8% of its initial capacity, confirming the exceptional structural integrity of KMnF-MC even at elevated temperatures.

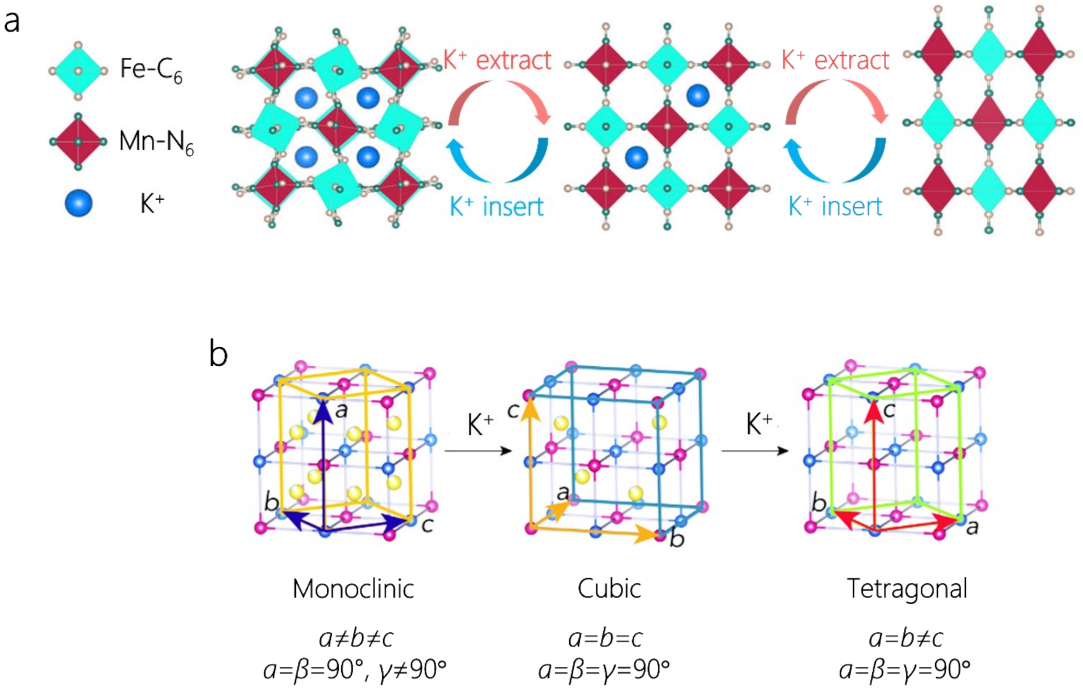

Figure S27. Schematic diagram of the crystal structure (a) and the corresponding unit cell (b) changes of KMnF during three phase transitions**.**

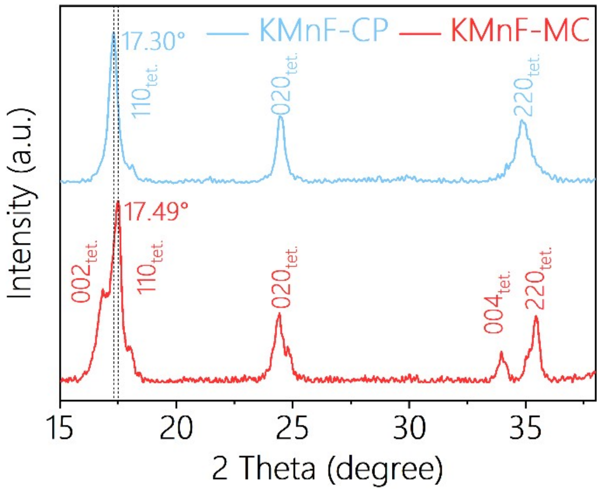

Figure S28. The XRD patterns of KMnF-CP and KMnF-MC at full charge.

According to Yang' studies[6, 7], the ideal tetragonal phase (without JTE) should satisfy the $a_{tet}/c_{tet} = \sqrt{2}/2$ (0.70711), and the deviation between the a_{tet}/c_{tet} value of actual tetragonal phase (fully charged) and the theoretical value (0.70711) can be used to determine the degree of octahedral distortion caused by JTE. The universal law of tetragonal unit cell parameters is as follows: a=b≠c, α=β=γ=90°. The actual volumes of unit cell in full charged state are 10.144Å×[7.174Å]^2 (KMnF-MC) and 10.238Å×[7.249]^2 (KMnF-CP), respectively. Obviously, the structure distortion of KMnF-MC (a_{tet}/c_{tet} =7.174/10.144 Å = 0.70722) is smaller than that of KMnF-CP a_{tet}/c_{tet} = 7.249/10.238 Å =0.70805), suggesting that Mn^{3+}-N_6 octahedral distortion from JTE for KMnF-MC may be milder. Notably, the (110) crystal plane of KMnF-MC is at a higher 2 theta value than that of KMnF-CP, which is because that more complete K^+ desertion ability results in a perfect tetragonal phase.

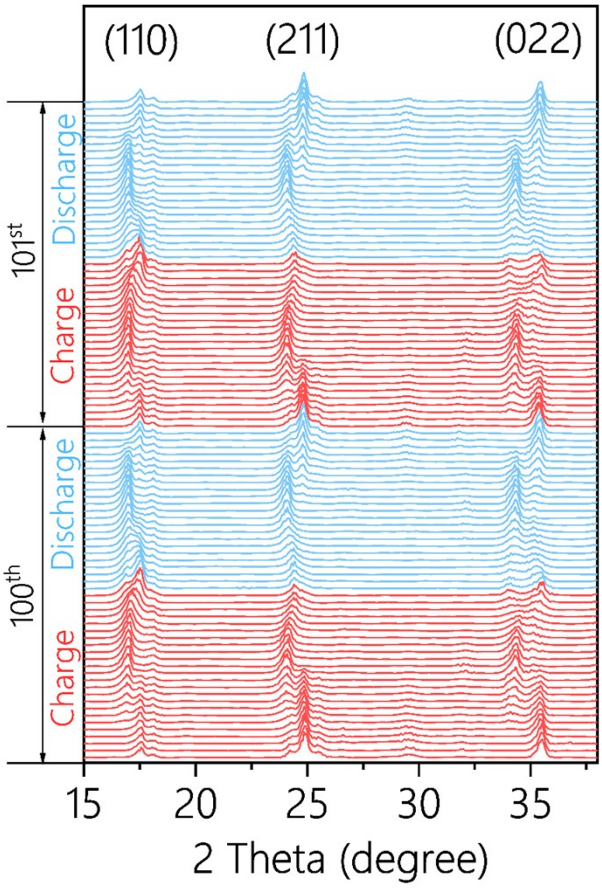

Figure S29. The in situ XRD patterns corresponding to 100 th and 101st cycles of KMnF-MC.

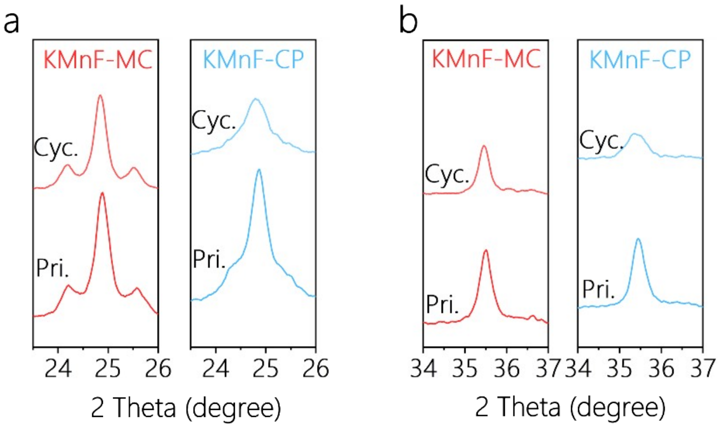

Figure S30. Local XRD patterns of the two samples after 100 cycles. (a) and (b) correspond to (211) and (022) planes, respectively

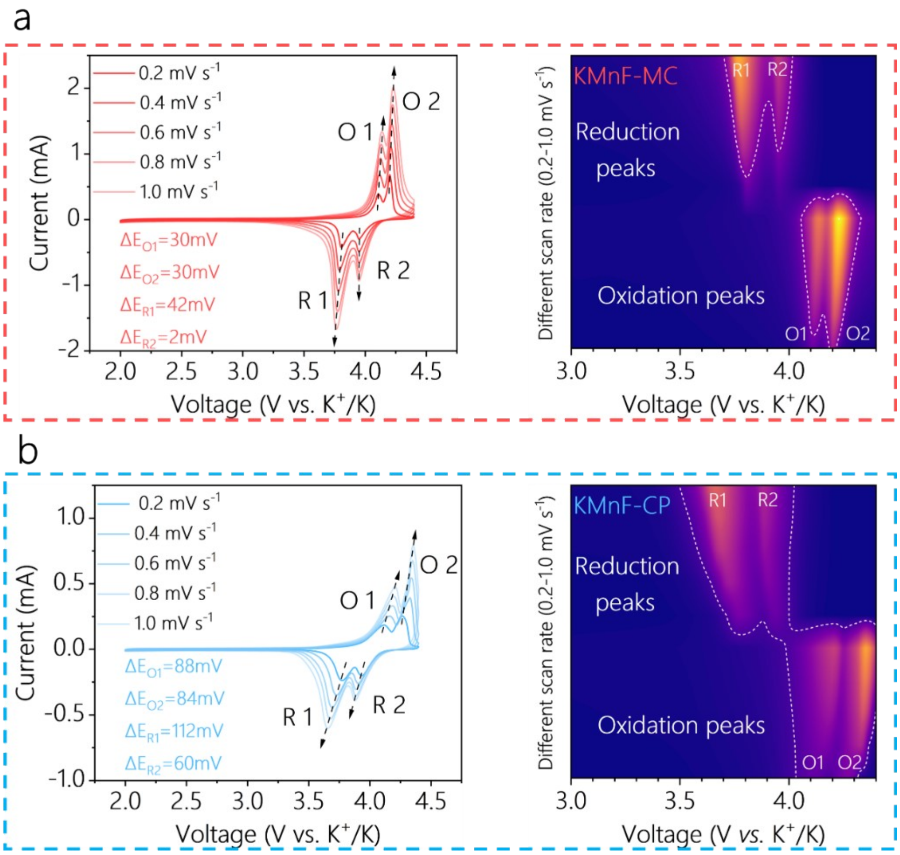

Figure S31. (a) and (b) Cyclic voltammetry curves of KMnF-MC and KMnF-CP at different scanning rates, respectively.

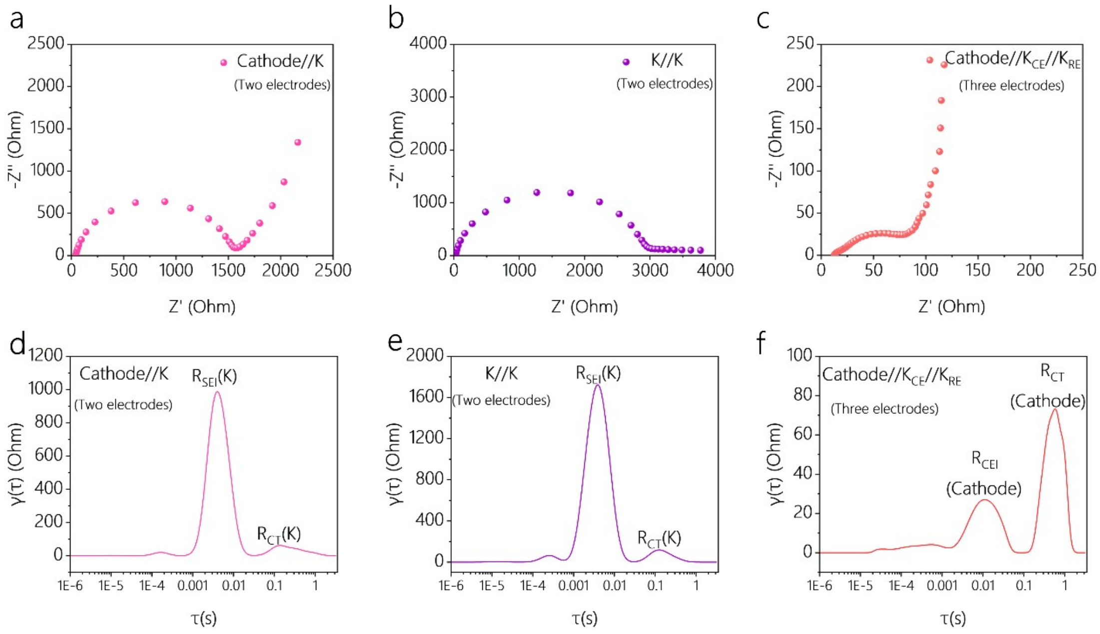

Figure S32. Identification of related time constant in DRT plots. (a-c) The EIS Nyquist plots using coin cells of Cathode///K (two-electrode cell), K//K (two-electrode cell), and Cathode//K$_{\text{counter electrode}}$//K$_{\text{reference electrode}}$ (three-electrode cell), respectively. (d-f) DRT plots obtained from EIS results, respectively.

As shown in Figure S32 (a) and (b), the impedance value of the PIBs reaches the order of 10^3, which is consistent with previous reports[8]. The huge impedance value actually results from the K^+ through the SEI and charge transfer process of the K metal anode (Figure S32 d and e). Unfortunately, information such as the charge transfer process at the cathode/electrolyte interface is often obscured. Therefore, we used a coin-type three-electrode cell to study the electrochemical kinetics of the cathode/electrolyte interface[9].

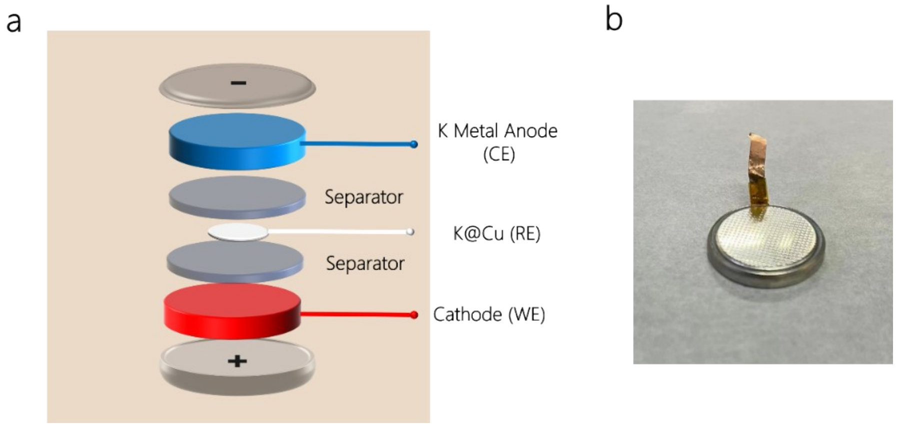

Figure S33. (a) Schematic diagram and (b) of the coin-type three-electrode cell.

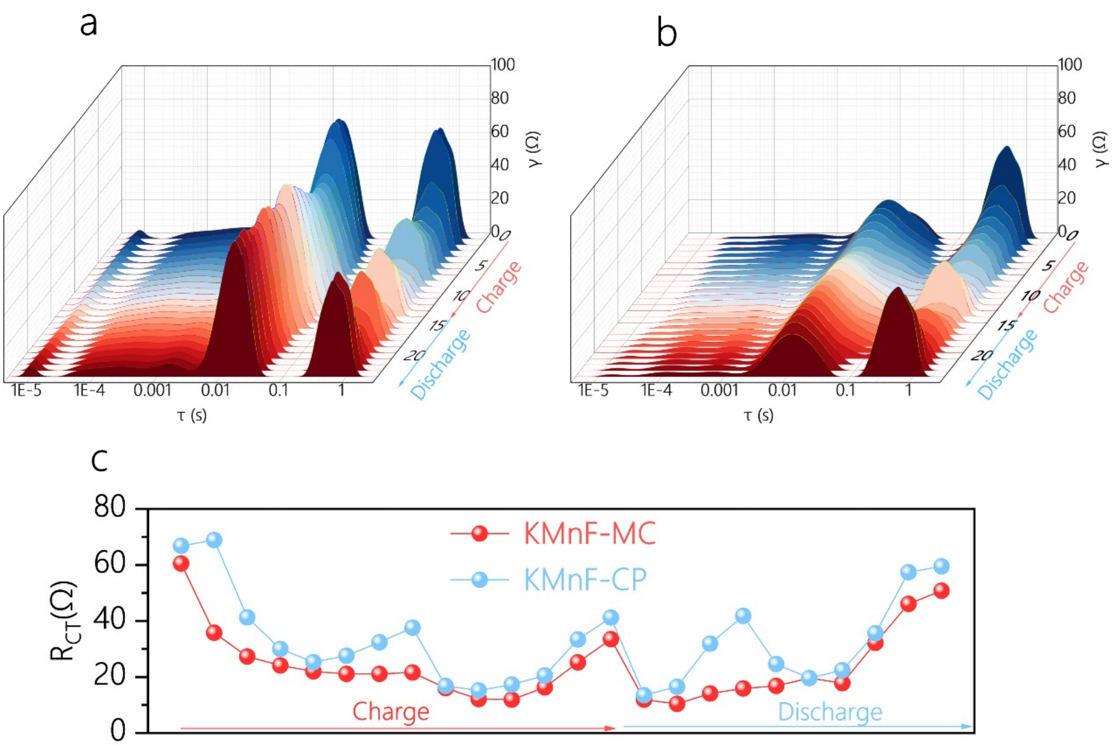

Figure S34. The in-situ EIS-DRT result of (a) KMnF-CP and (b) KMnF-MC. (c) Corresponding calculated impedances of charge transfer process.

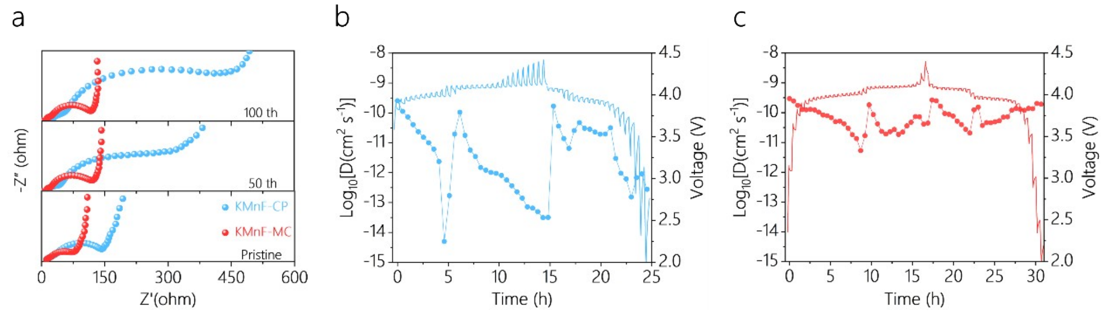

Figure S35. (a) The EIS Nyquist plots upon various cycles. GITT curves and calculated K^+ diffusion coefficients during 100th discharge–charge for (b) KMnF-CP and (c) KMnF-MC.

The EIS results show that the charge transfer process is hindered due to the severe damage of the KMnF-CP interface structure after long-term cycling, while the interface of KMnF-MC is well maintained, which is conducive to rapid ion transport and charge transfer. In addition, the D_{K^+} of KMnF-MC is similar to that of the initial state, while the D_{K^+} of KMnF-CP decreases significantly after cycling. This is due to the severe structure damage of KMnF-CP cathode, resulting in an increase in structural disorder and further hindering K^+ diffusion.

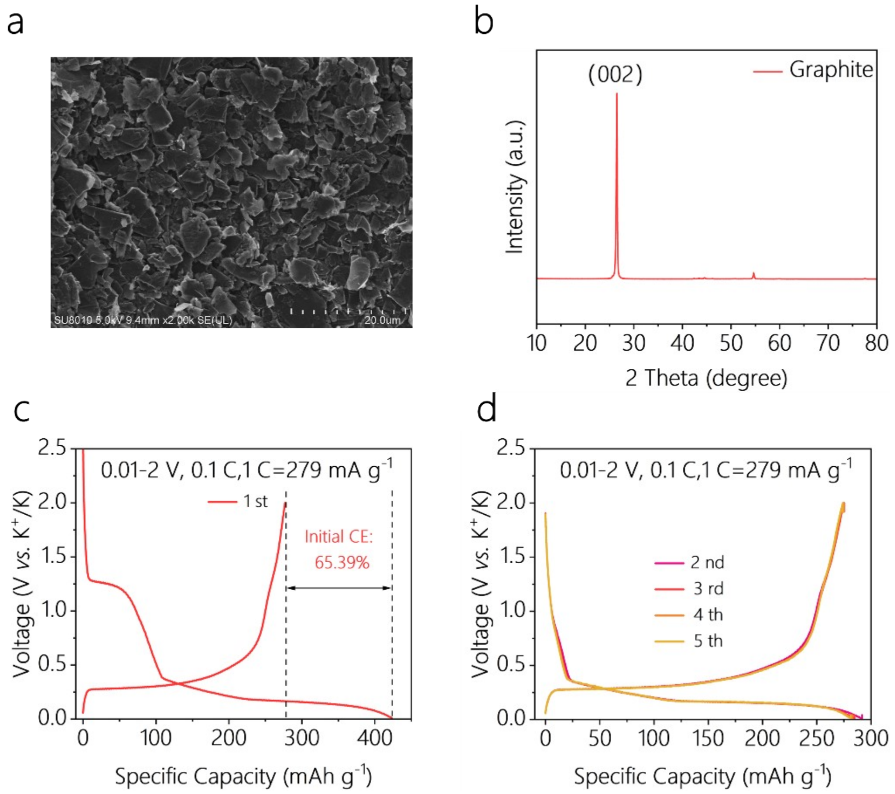

Figure S36. Graphite anode structure characterization and electrochemical performance testing. (a) The SEM images and (b) XRD pattern of Graphite. The voltage curves at 0.1 C (1 C=279 mA g^{-1}) of Graphite for (c) the first cycle and (d) the second to fifth cycles.

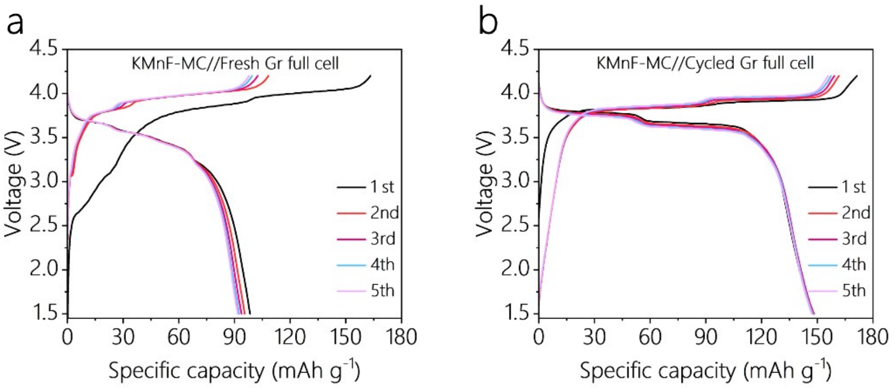

Figure S37. Charge–discharge profiles of the KMnF-MC//Gr full cell. (a) The full cell with a pristine Graphite anode; (b) The full cell with a cycled Graphite.

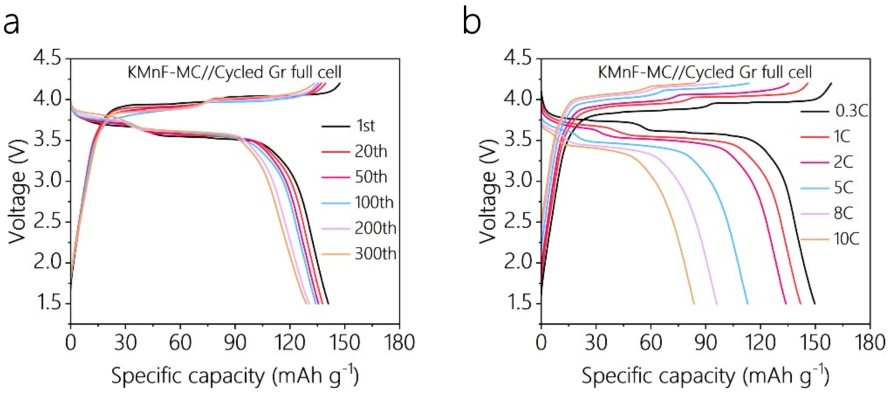

Figure S38. The KMnF-MC//cycled Gr full cell performance. (a) The cycling performance at 1 C charge/discharge rate within 300 cycles (after 0.3 C activation for 5 cycles); (b) The rate performance from 0.3 C to 10 C (1 C=150 mA g^{-1}).

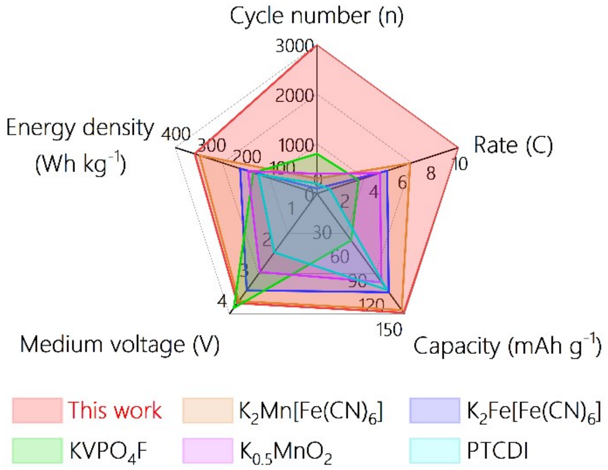

Figure S39. The specific capacity, discharge voltage, specific energy, cycle numbers and rate performance of KMnF-MC//cycled Gr full cell and other typical cycled-Gr-based K-ion full cell reported in the literature are compared[10-14].

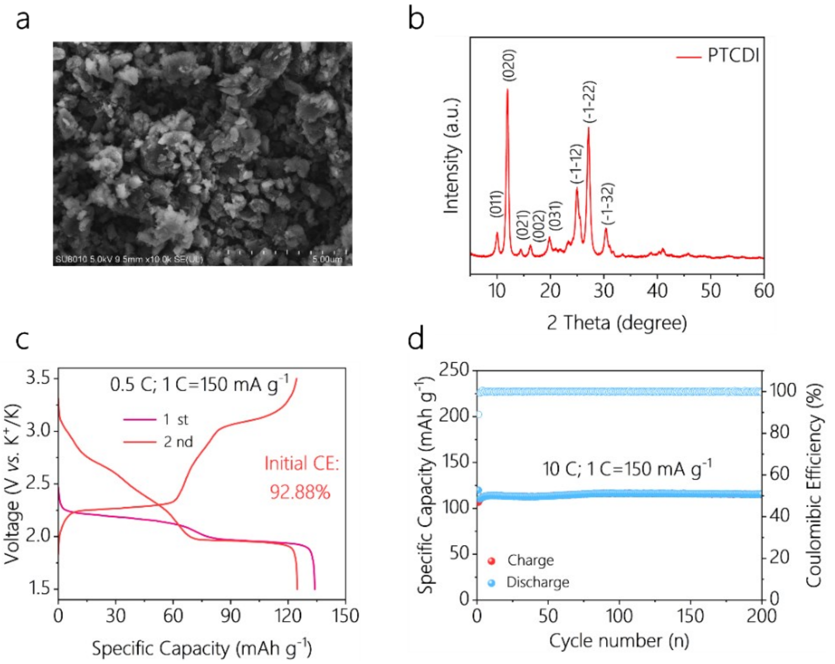

Figure S40. Structure characterization and electrochemical performance testing of PTCDI (Molecular formula: $C_{24}H_{10}N_2O_4$) anode. (a) The SEM image and (b) XRD pattern of PTCDI. (c) The voltage curves at 0.5 C (1 C=150 mA g^{-1}) of PTCDI and (d) the cycling performance at 10 C within 200 cycles.

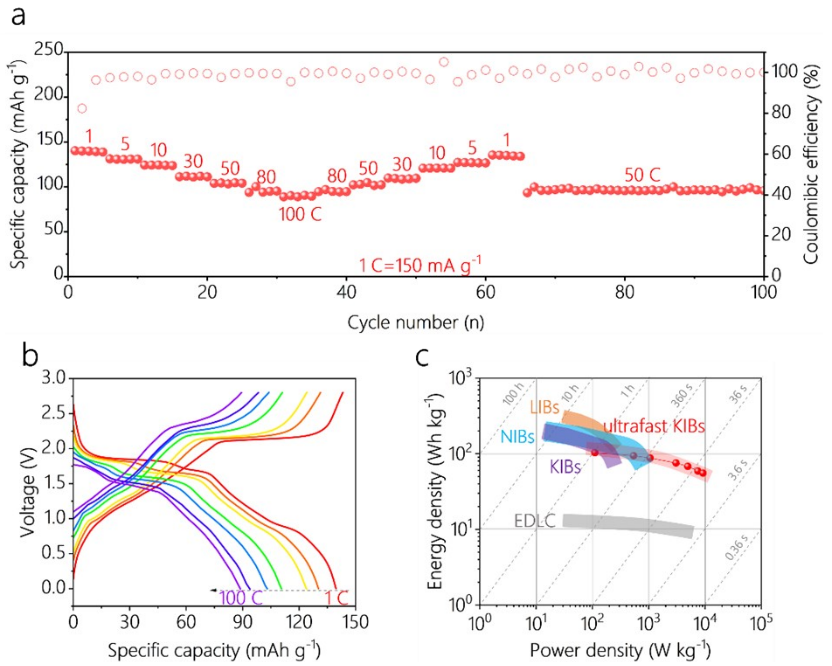

Figure S41. (a) and (b) The ultrahigh rate performance of the KMnF-MC//PTCDI full cell. (c) Ragone plot (energy density *vs.* power density).

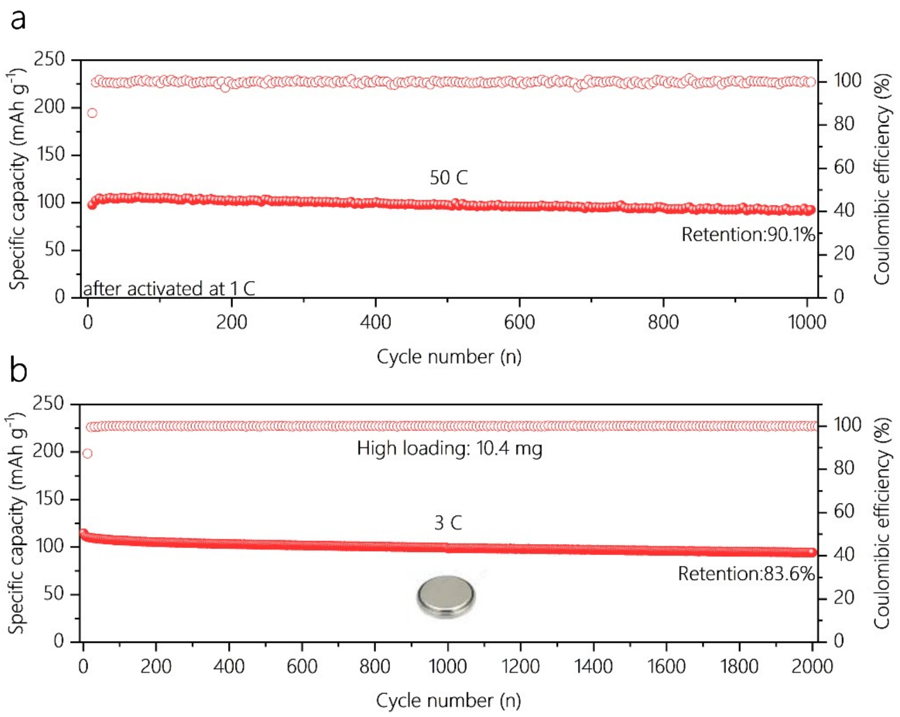

Figure S42. The cycling performance of KMnF-MC//PTCDI full cells at 50 C (a) and 10.4 mg/cm^2 (b), respectively.

KMnF-MC//PTCDI coin cells are assembled directly without additional K^+ supplementation and exhibit excellent rate performance and cycling stability. As shown in Figure S41, the capacity at 100 C is as high as 65% of that at 1 C (1C=150 mA g^{-1}), and the power density is up to 9,195 W kg^{-1}, which can realize the charging and discharging process in seconds and is expected to be applied in ultra-fast charging application scenarios. In addition, the KMnF-MC//PTCDI full cell also shows long-term cyclic stability at extremely conditions (ultrahigh current density or high mass loading), with a capacity retention of 90.1% after 1,000 cycles at 50 C, or with a retention of 83.6% after 2,000 cycles with 10.4 mg/cm^2 (Figure S42).

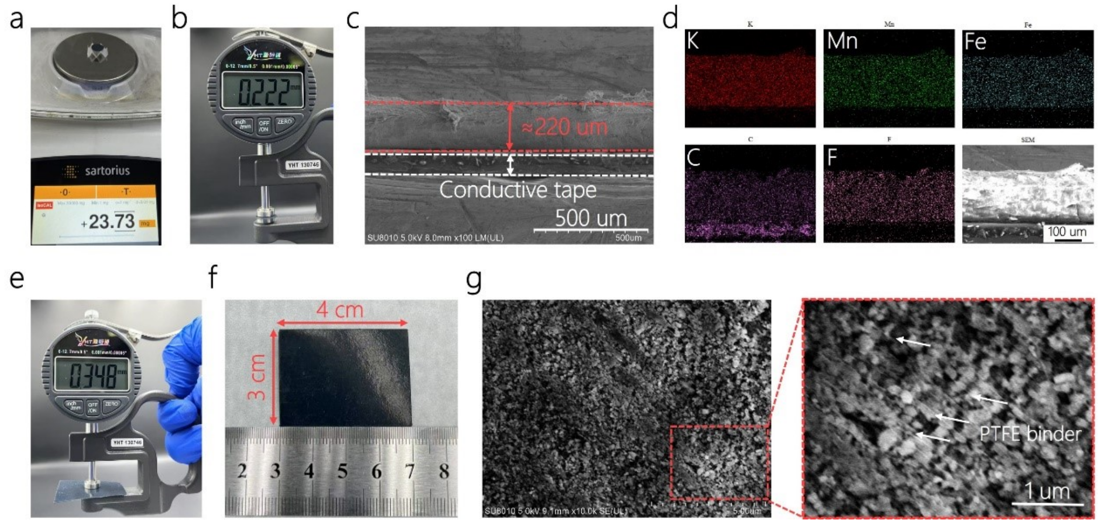

Figure S43. (a) The total mass and (b) thickness of the freestanding electrode film with a diameter of 12mm. (c) The SEM image and (d) the EDS elemental mappings of freestanding electrode film cross-section. (e) The total electrode thickness and (f) surface morphology of positive electrode (current collector included) for pouch cell. (g) The SEM images for microscopic morphology of positive electrode.

A 12 mm diameter disc freestanding KMnF-MC electrode film was cut and subjected to parametric testing. The electrode demonstrates a high active material loading of about 16.5 mg cm^{-2} (Figure S43a). In Figure S43b–e, the freestanding electrode film exhibited thicknesses of ~220 μm (before calendaring) and ~350 μm (after calendaring) containing the current collector in the pouch cell. The EDS elemental mapping confirms the homogeneous distribution of all components throughout the electrode thickness (Figure S43d). As depicted in Figure S43f and g, the electrode surface morphology is smooth and flat. Furthermore, the whole electrode shows that active materials and conductive additives are effectively connected by the PTFE binder while maintaining appropriate porosity to ensure sufficient electrolyte accessibility.

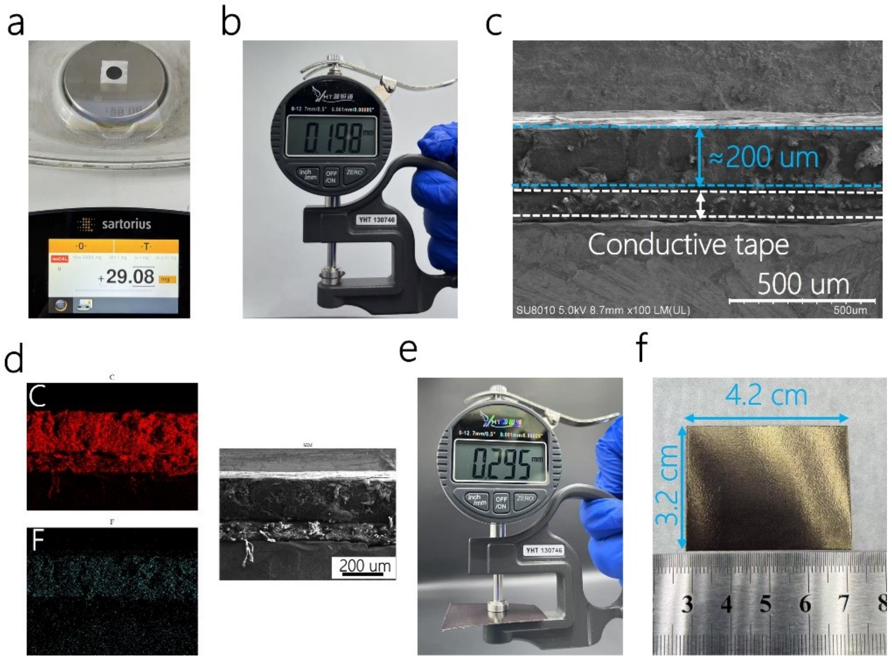

Figure S44. (a) The total mass and (b) thickness of the freestanding electrode film with a diameter of 12mm. (c) The SEM image and (d) the EDS elemental mappings of freestanding electrode film cross-section. (e) The total electrode thickness and (f) surface morphology of negative electrode (current collector included) for pouch cell.

As shown in Figure S44a–e, for the negative electrode with a high mass loading of 20.6 mg cm^{-2}, the freestanding electrode film exhibits thicknesses of ~200 μm (before calendaring) and ~300 μm (after calendaring) containing the current collector in the pouch cell. The negative electrode was fabricated with specific dimensions of 3.2 × 4.2 cm^2 - deliberately designed slightly larger than the cathode (3.0 × 4.0 cm^2) to avoid active K$^+$ loss at the edges during cycling (Figure S44f).

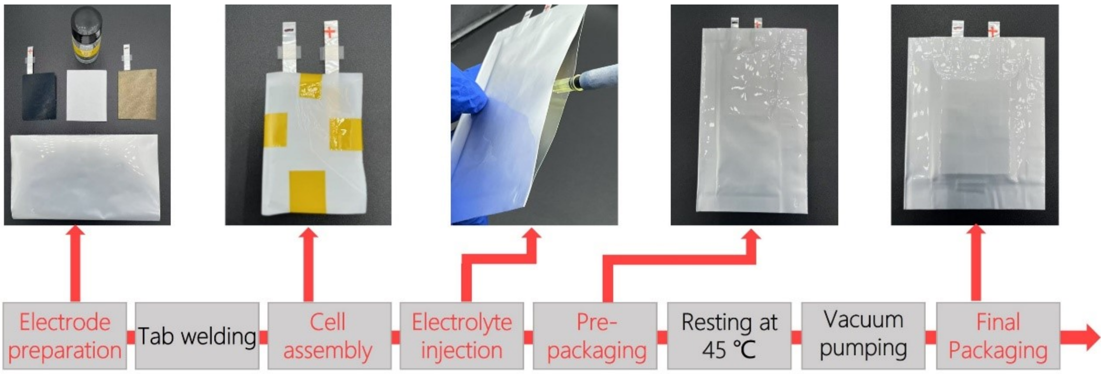

Figure S45. Assembly process flowchart of pouch cell.

Assembly Process Description:

(i) Electrode Stacking and Immobilization

The dry cell is assembled by sequentially stacking the positive electrode (KMnF-MC), separator (GF/A), and negative electrode (PTCDI), which are then fixed using chemically stable insulating films and adhesive tapes.

(ii) Pouch Pre-Packaging and Electrolyte Filling

The assembled stack is housed in laminated aluminum plastic film and subjected to three-edge thermal sealing, followed by electrolyte injection and preliminary encapsulation.

(iii) Electrolyte Wetting Process

The pre-sealed pouch cell undergoes a high-temperature aging process at 45°C to ensure complete electrolyte permeation throughout the electrode.

(iv) Final Packaging

The excess electrolyte and gas bubbles in the pouch cell were removed by vacuum pumping, followed by final packaging and trimming of the excess packaging material at the bottom.

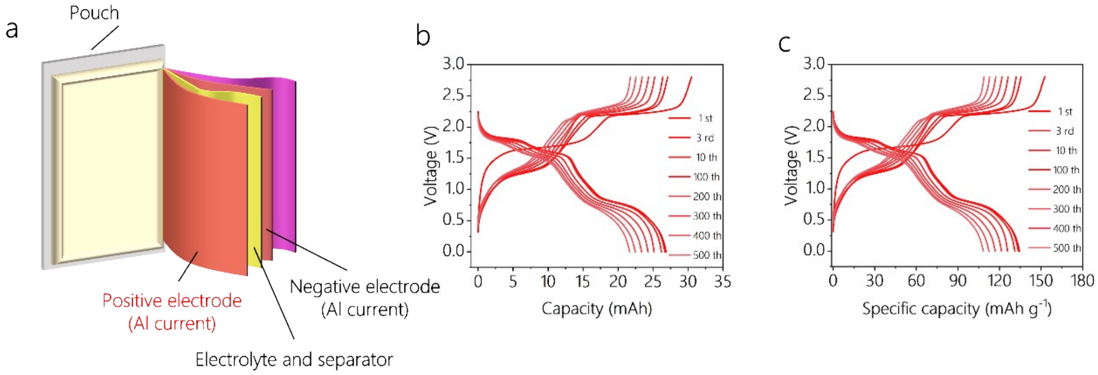

Figure S46. (a) Schematic diagram of pouch cell structure. (b) Capacity-voltage curves and (c) specific capacity-voltage curves of pouch cell.

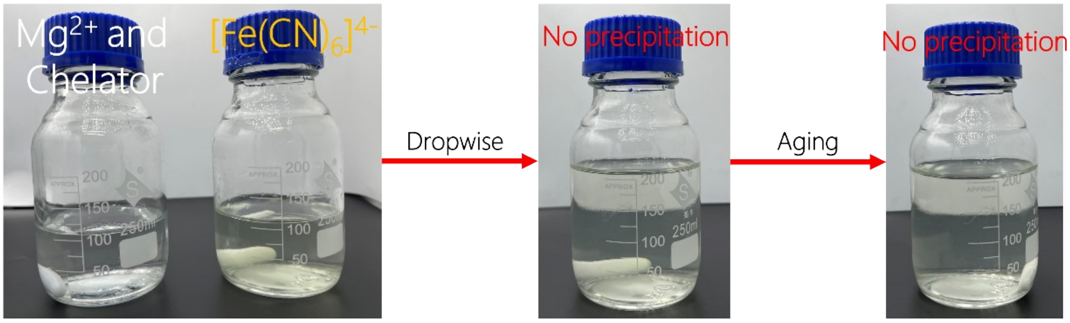

Figure S47. Digital photograph of the co-precipitation synthesis process of $K_2Mg[Fe(CN)_6]$.

Typically, the $K_2Mg[Fe(CN)_6]$ was synthesized via “co-precipitation” method as follows: 4 mmol Mg^{2+} (with 4mmol potassium citrate) and 4 mmol $Fe(CN)_6^{4-}$ were dissolved in 100 mL deionized (DI) water to obtain solution A and solution B respectively. Solution A was followed to be slowly added into solution B with magnetic stirring. Unfortunately, the $K_2Mg[Fe(CN)_6]$ precipitate was not obtained.

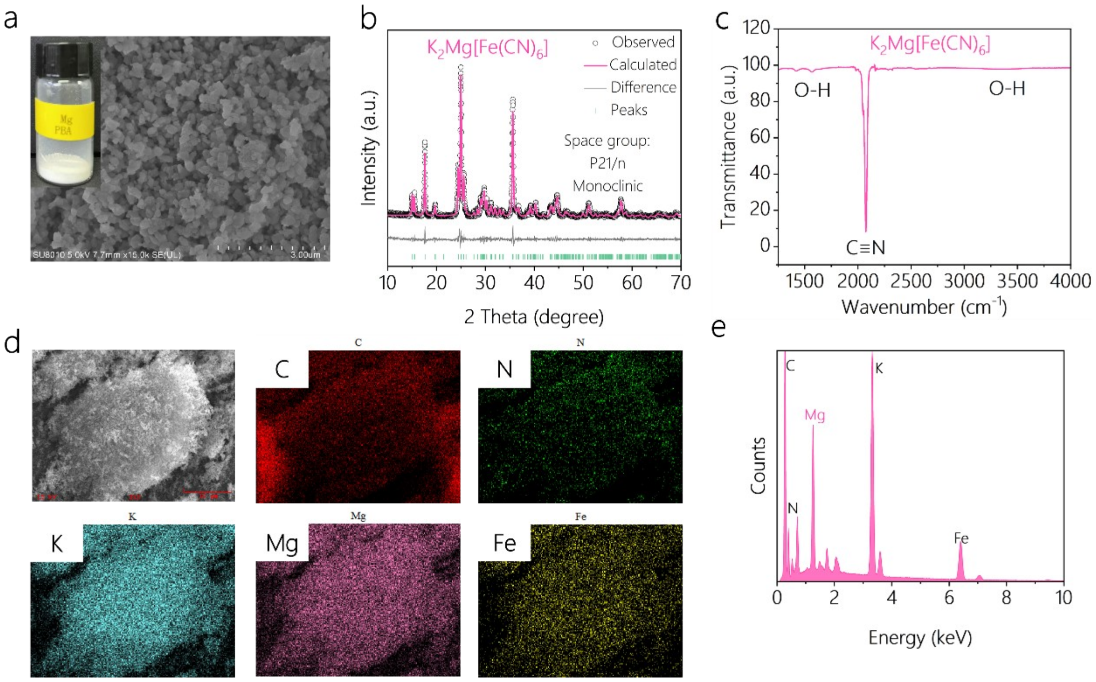

Figure S48. Structural characterization of mechanochemically prepared $K_2Mg[Fe(CN)_6]$. (a) The SEM images. Inset: digital photograph of the $K_2Mg[Fe(CN)_6]$ power. (b) The Rietveld-refined profiles and (c) FTIR spectra. (d) and (e) The EDS elemental mappings of the as-prepared $K_2Mg[Fe(CN)_6]$.

The $K_2Mg[Fe(CN)_6]$ prepared by high-energy ball milling showed good crystallinity and homogeneous nanoparticles. According to the result of ICP-OES, the chemical rules are calculated as: $K_{1.99}Mg[Fe(CN)_6]_{0.99}\cdot\square_{0.01}$.The XRD refinement results indicate that it has a potassium-rich monoclinic structure (space group of P21/n, a = 10.11450 Å, b = 7.31120 Å, c = 6.98860 Å, and β = 90.323°). The FTIR result shows that the obtained $K_2Mg[Fe(CN)_6]$ has extremely low peak intensity of O-H, indicating that there is almost no crystal water in the structure.

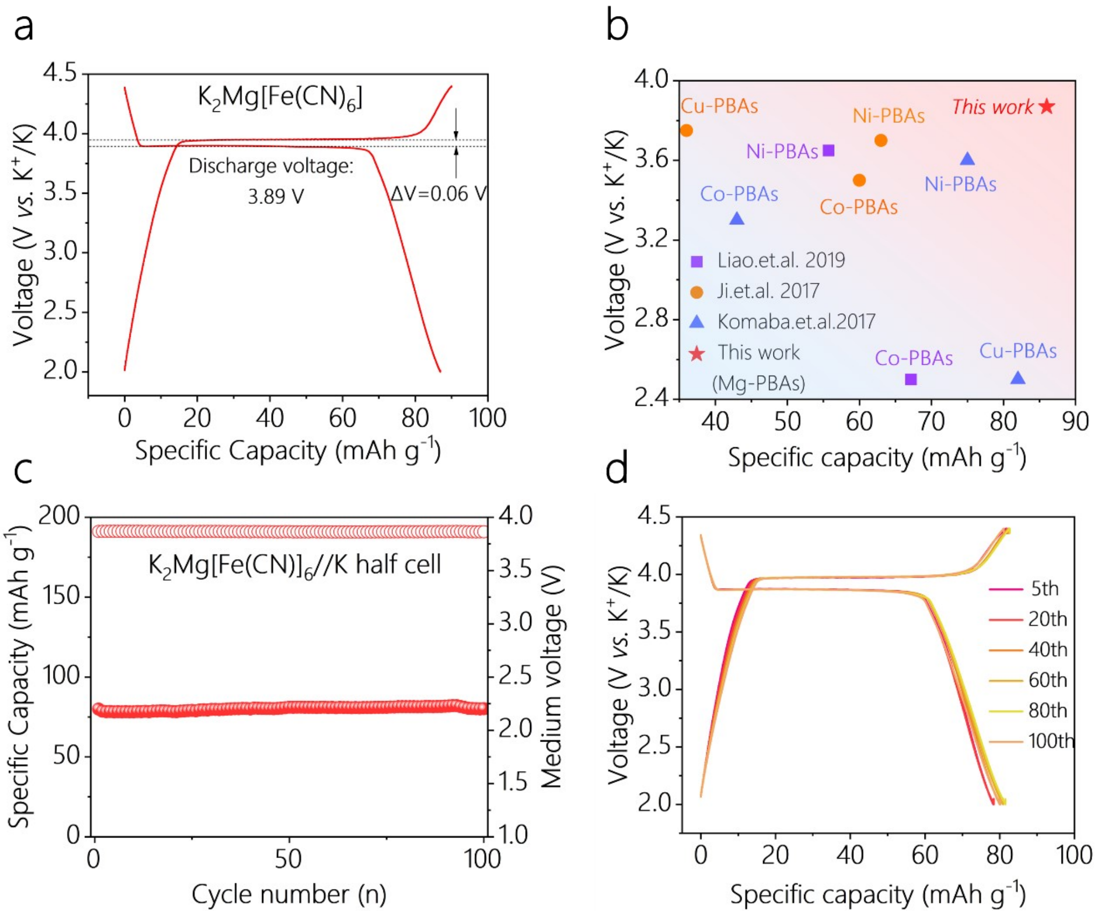

Figure S49. (a) Galvanostatic charge–discharge voltage profiles of $K_2Mg[Fe(CN)_6]$ at 10 mA g^{-1}. (b) Discharge voltage and specific capacity of some reported classical mono-redox active PBAs for PIBs[15-17].(c) and (d) The cycling stability at 50 mA g^{-1}.

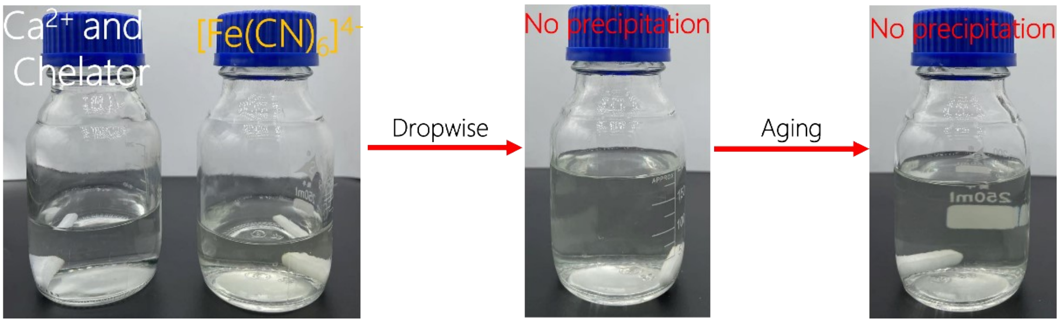

Figure S50. Digital photograph of the co-precipitation synthesis process of $K_2Ca[Fe(CN)_6]$.

Typically, the $K_2Ca[Fe(CN)_6]$ was synthesized via “co-precipitation” method as follows: 4 mmol Ca^{2+} (with 4mmol potassium citrate) and 4 mmol $Fe(CN)_6^{4-}$ were dissolved in 100 mL deionized (DI) water to obtain solution A and solution B respectively. Solution A was slowly added into solution B with magnetic stirring. Unfortunately, the $K_2Ca[Fe(CN)_6]$ precipitate was not obtained.

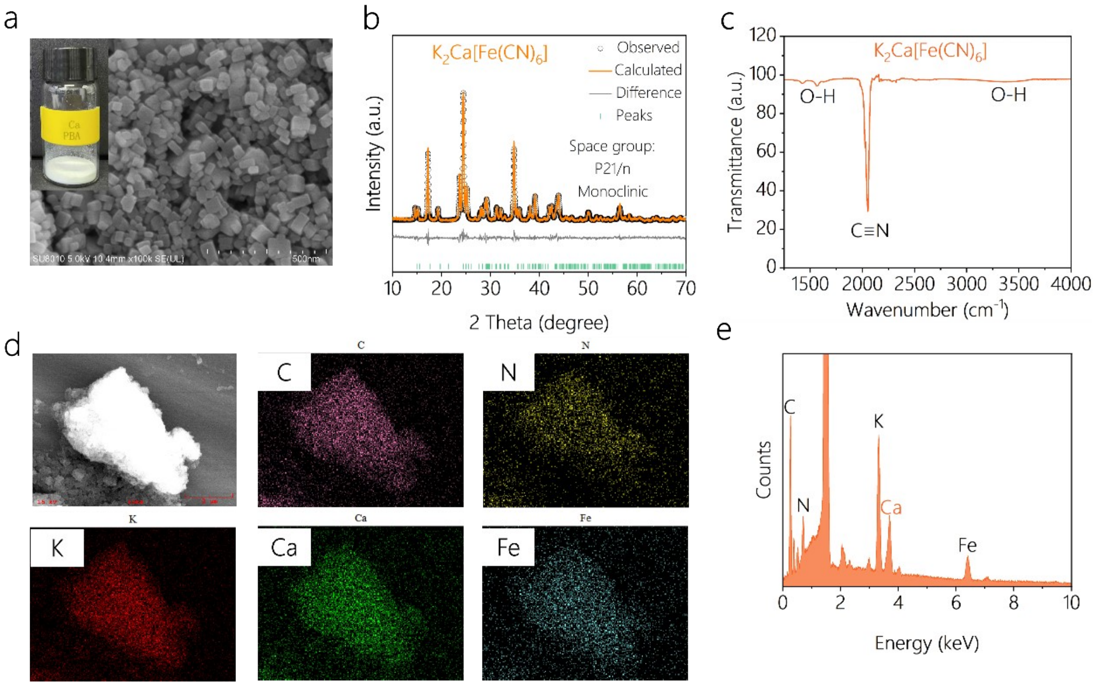

Figure S51. Structural characterization of mechanochemically prepared $K_2Ca[Fe(CN)_6]$. (a) The SEM images. Inset: digital photograph of the $K_2Ca[Fe(CN)_6]$ power. (b) The Rietveld-refined profiles and (c) FTIR spectra. (d) and (e) The EDS elemental mappings of the as-prepared $K_2Ca[Fe(CN)_6]$.

The $K_2Ca[Fe(CN)_6]$ prepared by high-energy ball milling showed good crystallinity and homogeneous nanoparticles. According to the result of ICP-OES, the chemical rules are calculated as: $K_{1.97}Ca[Fe(CN)_6]_{0.99}\cdot\square_{0.01}$.The XRD refinement results indicate that it has a potassium-rich monoclinic structure (space group of P21/n, a = 10.31160 Å, b = 7.51710 Å, c = 7.07990 Å, and β = 90.350°). The FTIR result shows that the obtained $K_2Ca[Fe(CN)_6]$ has extremely low peak intensity of O-H, indicating that there is almost no crystal water in the structure.

Table S1. ICP-OES results of as-prepared KMnF samples.

	K	Mn	Fe	Chemical formulas
KMnF-MC	1.98	1	0.98	$K_{1.98}Mn[Fe(CN)_6]_{0.98}\cdot\square_{0.02}$
KMnF-CP	1.71	1	0.89	$K_{1.71}Mn[Fe(CN)_6]_{0.89}\cdot\square_{0.11}$

Table S2. Structural parameters of the KMnF-MC sample obtained from Rietveld analysis.

S. G. P21/n a=10.13320 Å, b=7.35670 Å ,c=6.98200 Å, α=γ=90.00° , β=90.311°

Rp=4. 96%, Rwp=6.42%, Chi2=1.50

Atom	x	y	z	Occupancy	Wyckoff.
Fe	0.00000	0.00000	0.00000	1.000	2a
Mn	0.00000	0.50000	0.50000	1.000	2d
C1	0.53220	0.63660	0.26940	1.000	4e
C2	0.95840	0.78540	0.13270	1.000	4e
C3	0.68780	0.52040	0.56960	1.000	4e
N1	0.44880	0.26200	0.84880	1.000	4e
N2	0.05540	0.34610	0.75860	1.000	4e
N3	0.19660	0.47870	0.38590	1.000	4e
K	0.75290	0.93550	0.47670	0.985	4e

Table S3. Structural parameters of the KMnF-CP sample obtained from Rietveld analysis.

S. G. P21/n a=10.14200 Å, b=7.34220 Å ,c=7.03850 Å, α=γ=90.00° , β=89.584°

Rp=6. 05%, Rwp=7.86%, Chi2=2.03

Atom	x	y	z	Occupancy	Wyckoff.
Fe	0.00000	0.00000	0.00000	1.000	2a
Mn	0.00000	0.50000	0.50000	1.000	2d
C1	0.53110	0.64300	0.29100	1.000	4e
C2	0.93500	0.81200	0.26400	1.000	4e
C3	0.66800	0.48300	0.54900	1.000	4e
N1	0.44950	0.25250	0.84870	1.000	4e
N2	0.04500	0.35800	0.77600	1.000	4e
N3	0.20920	0.47670	0.40700	1.000	4e
K	0.76080	0.93440	0.45870	0.899	4e

Table S4. Comparison the specific capacity, discharge voltage and energy density of the typical cathode for PIBs in literatures.

Cathodes	Specific capacity (mAh g^{-1})	Discharge voltage (V)	Energy density (Wh kg^{-1})
ADQS[18]	101 (10 mA g^{-1}, 0.1 C)	1.98	200
PTCDA[19]	147 (20 mA g^{-1}, 0.14 C)	2.38	350
VO_2[20]	107 (20 mA g^{-1}, 0.19 C)	2.01	214
$K_{0.5}MnO_2$[13]	127 (20 mA g^{-1}, 0.16 C)	2.96	376
$K_{0.6}CoO_2$ [21]	81 (10 mA g^{-1}, 0.13 C)	2.75	223
$K_{0.5}VOPO_4$[22]	118 (20 mA g^{-1}, 0.17 C)	3.40	401
$KVPO_4F$ [12]	96 (20 mA g^{-1}, 0.2 C)	4.01	385
$KFeSO_4F$ [23]	120 (24 mA g^{-1}, 0.2 C)	3.60	432
Ni-PBA [24]	57 (10 mA g^{-1}, 0.18 C)	3.74	213
Fe-PBA [11]	124 (20 mA g^{-1}, 0.16 C)	3.58	444
This work	**149 (30 mA g^{-1}, 0.2 C)**	**3.96**	**590**

Table S5. Comparison the rate performance of the typical cathode for PIBs in literatures.

Cathodes	Current density (Min and Max, mA g^{-1})	Specific capacity (Max and Min, mAh g^{-1})
$K_{1.994}Mn[Fe(CN)_6]_{0.994}$[10]	30, 500	137, 74
$KVPO_4F$-PVDF[12]	50, 1000	95, 48
$KFeC_2O_4F$[27]	100, 500	130, 88
$K_{0.7}Mn_{0.67}Ni_{0.33}O_2$[25]	10, 500	117, 73
P2-$K_{0.6}CoO_2$[28]	25, 500	83, 31
VO_2[20]	20, 500	107, 70
$K_{1.82}Mn[Fe(CN)_6]_{0.98}$[26]	20, 3000	140, 23
This work	**30, 7500**	**149, 78**

Table S6. The change of FWHM before and after cycles.

	(110)	(211)	(022)
KMnF-CP (Pristine)	0.31°	0.51°	0.39°
KMnF-CP (100 cycles)	0.44°	0.58°	0.49°
KMnF-MC (Pristine)	0.27°	0.44°	0.35°
KMnF-MC (100 cycles)	0.28°	0.46°	0.36°

Table S7. The energy density and cycling performance of typical reported K-ion full cells based on cathodes.

Positive electrode	Negative electrode	Discharge Voltage	Energy density	Cycling performance
PTCDA	Gr	2.3	167 Wh kg^{-1} (100 mA g^{-1})	81.5% after 50 cycles (100 mA g^{-1})
PTCDA	Gr	2.2	143.6 Wh kg^{-1} (20 mA g^{-1})	80% after 150 cycles (100 mA g^{-1})
PTCDA	Gr	1.7	140.6 Wh kg^{-1} (100 mA g^{-1})	83.3% after 200 cycles (100 mA g^{-1})
PTCDA	KC8	2.3	146.7 Wh kg^{-1} (50 mA g^{-1})	86.8% after 300 cycles (100 mA g^{-1})
NMCTO	Gr	2.6	198.9 Wh kg^{-1} (20 mA g^{-1})	83.9% after 150 cycles (200 mA g^{-1})
P2-$K_{0.6}CoO_2$	SC	2.8	143.6 Wh kg^{-1} (20 mA g^{-1})	78.8% after 300 cycles (20 mA g^{-1})
$K_{0.7}Mn_{0.7}Ni_{0.3}O_2$	SC	2.2	82.4 Wh kg^{-1} (100 mA g^{-1})	62.5% after 300 cycles (300 mA g^{-1})
$K_{0.5}MnO_2$	Gr	2.7	194.6 Wh kg^{-1} (20 mA g^{-1})	83% after 400 cycles (500 mA g^{-1})
$KFeC_2O_4F$	SC	2.9	176.6 Wh kg^{-1} (100 mA g^{-1})	100% after 200 cycles (100 mA g^{-1})
$KVPO_4F$	SC	3.7	235.5 Wh kg^{-1} (50 mA g^{-1})	80.3% after 500 cycles (50 mA g^{-1})
$KFeSO_4F$	Gr	3.5	243 Wh kg^{-1} (100 mA g^{-1})	89.5% after 600 cycles (100 mA g^{-1})
$KVPO_4F$	Gr	3.8	242.8 Wh kg^{-1} (20 mA g^{-1})	81.3% after 800 cycles (300 mA g^{-1})

$K_2Fe[Fe(CN)_6]$	Gr	2.9	216.7 Wh kg^{-1} (20 mA g^{-1})	97.4% after 100 cycles (100 mA g^{-1})
$K_2Mn[Fe(CN)_6]$	Gr	3.5	226.5 Wh kg^{-1} (50 mA g^{-1})	98.3% after 300 cycles (200 mA g^{-1})
$K_2Mn[Fe(CN)_6]$	Gr	3.6	331.5 Wh kg^{-1} (15 mA g^{-1})	98.5% after 300 cycles (30 mA g^{-1})
$K_2Ni[Fe(CN)_6]$	Gr	2.8	69.9 Wh kg^{-1} (100 mA g^{-1})	87.1% after 500 cycles (500 mA g^{-1})
$K_2Mn[Fe(CN)_6]$ **(This work)**	**Gr**	**3.6 V**	**326 Wh kg^{-1}** (45 mA g^{-1})	**91.5% after 300 cycles** **(150 mA g^{-1})** **84.5% after 3,000 cycles** **(750 mA g^{-1})**

References

[1] L. L. Driscoll, E. H. Driscoll, B. Dong, F. N. Sayed, J. N. Wilson, C. A. O'Keefe, D. J. Gardner, C. P. Grey, P. K. Allan, A. A. L. Michalchuk, P. R. Slater, *Energy Environ. Sci.* **2023**, *16*, 5196-5209.

[2] O. Maus, M. A. Lange, F. Frankenberg, F. Stainer, V. Faka, E. Schlautmann, C. Rosenbach, A. Jodlbauer, J. Schubert, J. Janek, C. Li, P. Michalowski, H. M. R. Wilkening, A. Kwade, W. G. Zeier, *Adv. Energy Mater.* **2024**.

[3] L. Jiang, Y. Lu, C. Zhao, L. Liu, J. Zhang, Q. Zhang, X. Shen, J. Zhao, X. Yu, H. Li, X. Huang, L. Chen, Y.-S. Hu, *Nat. Energy* **2019**, *4*, 495-503.

[4] Z. Zhang, M. Avdeev, H. Chen, W. Yin, W. H. Kan, G. He, *Nat. Commun.* **2022**, *13*, 7790.

[5] L. Ge, Y. Song, P. Niu, B. Li, L. Zhou, W. Feng, C. Ma, X. Li, D. Kong, Z. Yan, Q. Xue, Y. Cui, W. Xing, *ACS Nano* **2024**, *18*, 3542-3552.

[6] S. Li, H. Zhu, Y. Liu, Z. Han, L. Peng, S. Li, C. Yu, S. Cheng, J. Xie, *Nat. Commun.* **2022**, *13.*

[7] Y. Shang, X. Li, J. Song, S. Huang, Z. Yang, Z. J. Xu, H. Y. Yang, *Chem* **2020**, *6*, 1804-1818.

[8] M. Hamada, R. Tatara, K. Kubota, S. Kumakura, S. Komaba, *ACS Energy Letter.* **2022**, *7*, 2244-2246.

[9] C. Gao, M. Chen, J. Li, X. Wang, G. Zhang, X. Tan, S. Zhang, G. Feng, D. Zhai, F. Kang, *Energy Environ. Sci.* **2024**.

[10] L. Deng, J. Qu, X. Niu, J. Liu, J. Zhang, Y. Hong, M. Feng, J. Wang, M. Hu, L. Zeng, Q. Zhang, L. Guo, Y. Zhu, *Nat. Commun.* **2021**, *12*, 2167.

[11] A. Li, Y. Man, J. Liao, L. Duan, X. Ji, X. Zhou, *Nano Letter.* **2023**, *23*, 10066-10073.

[12] Q. Fu, W. Zhou, P. Gao, H. Dong, S. Chen, C. Fan, J. Liu, *Energy Environ. Sci.* **2024**, *17*, 5147-5161.

[13] L. Deng, T. Wang, Y. Hong, M. Feng, R. Wang, J. Zhang, Q. Zhang, J. Wang, L. Zeng, Y. Zhu, L. Guo, *ACS Energy Letter.* **2020**, *5*, 1916-1922.

[14] X. Yi, H. Fu, A. M. Rao, Y. Zhang, J. Zhou, C. Wang, B. Lu, *Nat. Sustain.* **2024**, *7*,

326-337.

[15] X. Bie, K. Kubota, T. Hosaka, K. Chihara, S. Komaba, *J. Mater. Chem. A* **2017**, *5*, 4325-4330.

[16] X. Wu, Z. Jian, Z. Li, X. Ji, *Electrochem. Commun.* **2017**, *77*, 54-57.

[17] B. Huang, Y. Shao, Y. Liu, Z. Lu, X. Lu, S. Liao, *ACS Appl. Energy Mater.* **2019**, *2*, 6528-6535.

[18] B. Li, J. Zhao, Z. Zhang, C. Zhao, P. Sun, P. Bai, J. Yang, Z. Zhou, Y. Xu, *Adv. Funct. Mater.* **2018**, *29*.

[19] Y. Zhao, S. Sui, Q. Yang, J. Li, S. Chu, M. Gu, L. Li, S. Shi, Y. Zhang, Z. Chen, S. Chou, K. Lei, *Nano Letter.* **2024**, *24*, 4546-4553.

[20] L. Wu, H. Fu, S. Li, J. Zhu, J. Zhou, A. M. Rao, L. Cha, K. Guo, S. Wen, B. Lu, *Nat. Commun.* **2023**, *14*.

[21] T. Deng, X. Fan, C. Luo, J. Chen, L. Chen, S. Hou, N. Eidson, X. Zhou, C. Wang, *Nano Lett* **2018**, *18*, 1522-1529.

[22] H. Li, J. Dong, D. Han, J. Hu, X. Li, F. Kang, D. Zhai, *ACS Appl. Energy Mater.* **2020**, *4*, 445-451.

[23] Y. Liu, Z.-Y. Gu, Y.-L. Heng, J.-Z. Guo, M. Du, H.-J. Liang, J.-L. Yang, K.-Y. Zhang, K. Li, X.-L. Wu, *Green Energy & Environ.* **2024**, *9*, 1724-1733.

[24] S. Chong, Y. Wu, S. Guo, Y. Liu, G. Cao, *Energy Storage Mater.* **2019**, *22*, 120-127.

[25] L. Duan, C. Shao, J. Liao, L. Song, Y. Zhang, R. Li, S. Guo, X. Zhou, H. Zhou, *Angew. Chem. Int. Ed.* **2024**.

[26] X. Li, T. Guo, Y. Shang, T. Zheng, B. Jia, X. Niu, Y. Zhu, Z. Wang, *Adv. Mater.* **2024**, *36*.

[27] B. Ji, W. Yao, Y. Zheng, P. Kidkhunthod, X. Zhou, S. Tunmee, S. Sattayaporn, H. M. Cheng, H. He, Y. Tang, *Nat. Commun.* **2020**, *11*, 1225.

[28] Z. Zhang, Q. Hu, J. Liao, Y. Xu, L. Duan, R. Tian, Y. Du, J. Shen, X. Zhou, *Nano Lett.* **2023**, *23*, 694-700.